# Attitude profiles for ground-path pointing and alignment of radar footprints: Application to the INCUS mission

*Original*
Attitude profiles for ground-path pointing and alignment of radar footprints: Application to the INCUS mission / Martire, Paolo; Kostelecky, Quinn; Boudad, Kenza; Tanelli, Simone; Battaglia, Alessandro. - In: ACTA ASTRONAUTICA. - ISSN 0094-5765. - 240:(2026), pp. 581-599. [10.1016/j.actaastro.2025.12.019]

*Publisher:*
Elsevier

*Published*
DOI:10.1016/j.actaastro.2025.12.019

Acta Astronautica 240 (2026) 581–599

Contents lists available at ScienceDirect

Acta Astronautica

journal homepage: www.elsevier.com/locate/actaastro

Research Paper

# Attitude profiles for ground-path pointing and alignment of radar footprints: Application to the INCUS mission

Paolo Martire [a],*, Quinn Kostelecky [b], Kenza Boudad [b], Simone Tanelli [b], Alessandro Battaglia [c]

[a] Department of Mechanical and Aerospace Engineering, Politecnico di Torino, Corso Duca degli Abruzzi 24, 10129, Turin, Italy
[b] Jet Propulsion Laboratory, California Institute of Technology, 4800 Oak Grove Dr., 91109, Pasadena, CA, USA
[c] Department of Environment, Land and Infrastructure Engineering, Politecnico di Torino, Corso Duca degli Abruzzi 24, 10129, Turin, Italy

## ARTICLE INFO

*Keywords:*
Attitude guidance
Ground-path pointing
Radar footprint
Earth observation
Satellite constellation

## ABSTRACT

This work presents the derivation of pointing profiles for a satellite mission requiring continuous observations of a ground path. The study is directly applied to the INvestigation of Convective Updrafts (INCUS) mission, a three-satellite constellation designed to investigate tropical convective storms through time-differenced radar observations. A sequence of pitch, roll, and yaw rotations was investigated to align each spacecraft with the reference ground path, while accounting for mission-specific requirements and constraints. A pointing strategy with fixed pitch and time-varying roll was examined to achieve ground-path pointing. A subsequent yaw rotation was then studied to ensure correct cross-track alignment of the radar footprints. A numerical search-strategy was performed to derive the time difference between observations and the pointing profiles, while an additional analytical formulation was also developed to address the footprint alignment problem. The effects of in-track spacecraft knowledge position errors on both the pointing profiles and cross-track alignment of the footprints were also investigated. Moreover, the effects of variations in orbital inclination and altitude on the pointing profiles have been addressed.

## 1. Introduction

Many Earth-observing space missions are required to continuously point their payloads or instruments towards specific locations on Earth for extended periods of time. This requirement translates into orienting the spacecraft so that an axis of interest — such as an antenna boresight — is directed towards the desired location on Earth. Several studies have addressed the problem of ground–target tracking for various applications. A general method for autonomous tracking is presented in [1], where the spacecraft is commanded to point a body-fixed axis to a specific location on Earth, while minimizing the amplitude of the desired angular velocity. A similar problem is tackled in [2], where a spacecraft is required to point a spaceborne camera towards a fixed point on ground for real-time video monitoring. Both the staring attitude and angular velocity are derived, with the former characterized by a zero-yaw angle throughout the entire process to ensure minimal image distortion. A sunlight-reflection staring mode is discussed in [3], in which the spacecraft is controlled to reflect sunlight towards a designated ground location when the required geometric conditions are satisfied. A general derivation of the staring attitude is presented in [4], in which the degree of freedom about the pointing axis is constrained by selecting among various criteria, such as minimizing the rotation angle with respect to a given reference frame, minimizing the deviation angle between two specified vectors, minimizing angular velocity, or satisfying additional payload constraints. Among other applications, satellite attitude maneuvering has been investigated to enable specific scanning modes in spaceborne synthetic aperture radar systems. In [5], an attitude maneuver scheme was proposed to achieve sliding spotlight mode, in which the antenna boresight is directed towards a designated virtual rotation center to enable azimuth beam steering and improve azimuth resolution. In [6], an attitude maneuvering strategy was analyzed to image multiple closely spaced targets in both staring and sliding spotlight modes, while minimizing retargeting time between consecutive target observations. In a similar vein, a general real-time attitude guidance planner for consecutive target observation with near-optimal retargeting time minimization was presented in [7]. Aside from the different applications, the common pointing mode among the cited studies involves staring at a single or a few consecutive fixed ground

---

* Corresponding author.
*E-mail addresses:* paolo.martire@polito.it (P. Martire), quinn.kostelecky@jpl.nasa.gov (Q. Kostelecky), kenza.boudad@gmail.com (K. Boudad), simone.tanelli@jpl.nasa.gov (S. Tanelli), alessandro.battaglia@polito.it (A. Battaglia).

https://doi.org/10.1016/j.actaastro.2025.12.019
Received 26 August 2025; Received in revised form 21 November 2025; Accepted 9 December 2025

targets for a certain period. To the best of the authors' knowledge, no relevant studies have been found addressing spacecraft attitude maneuvers aimed at tracking a continuous ground path. Falling within the latter category, the present study investigates ground-path pointing through attitude maneuvering, with direct application to the INCUS mission.

The Investigation of Convective Updrafts (INCUS) is a NASA Earth Venture Mission aimed at enhancing our understanding of how tropical convective storms form [8]. INCUS's core interest is the vertical transport of water and air in convective storms, known as convective mass flux (CMF). CMF plays a crucial role in weather and climate systems, and a global quantitative assessment of its impact on several atmospheric phenomena is pivotal to the atmospheric science community. Estimates of CMF can be obtained from time-differenced radar reflectivity measurements acquired by microwave radars [9]. Based on this notion, the INCUS mission employs a constellation of three spacecraft to perform measurements of time-differenced radar reflectivity from Low Earth Orbit (LEO). The three spacecraft are deployed in the same orbit, with time separations of 30 s between the first and the second, and 120 s between the first and the third. Each of the three spacecraft is equipped with a Dynamic Atmospheric Radar (DAR), with one of the three also carrying a Dynamic Microwave Radiometer (DMR). Each DAR can generate seven sequentially activated, partially overlapping beams near nadir, whose 3 dB footprints are required to overlap by 2/3 in the cross-track direction (i.e., the 4th beam in the sequence is the central beam, with beams 2 and 6 at the edges of the swath, following the numbering identifiers shown in Fig. 1), resulting in a total swath width of approximately 9 km [10]. Given the near vertical viewing geometry and accounting for the DAR range resolution of approximately 120 m, each of the 7 beams on each of the 3 spacecraft produces near-vertical sections of the troposphere (typically referred to as 'curtain plots') as it moves along its trajectory. The resulting observation from each spacecraft is a 3-D depiction of condensate in the storms. These are then compared across the 3 spacecrafts to observe the movement of condensate inside a storm (in essence producing 3 consecutive 3-D frames of the evolving storm within 120 s). Therefore, the INCUS constellation will be able to make systematic in-cloud observations of weather systems at the timescale required to capture their nonlinear dynamic [11], and with the necessary spatial resolution. To enable continuous time-differenced observations of the same three-dimensional atmospheric regions, the three spacecraft must be oriented towards a common Earth-fixed reference path. In addition, DAR's footprints must be properly arranged around this reference path to achieve the desired overlap and swath width. As described in the following sections, ground-path pointing is achieved through a sequence of pitch and roll rotations, while a yaw rotation is applied to align the footprints. A numerical search strategy was applied to derive the pointing profiles and the time difference between observations. In the present study we assume each spacecraft is capable of directly tracking a series of aimpoints uplinked from ground stations, while it lacks the ability to generate the yaw profile onboard (which must therefore be computed on ground and uplinked to the spacecraft). Motivated by this, an analytical formulation was explored to derive a general law for the yaw, given the aimpoint locations and the spacecraft's attitude and position. It is shown that the footprint alignment problem can be formulated as a boundary value problem; however, it does not admit a simple closed-form solution. When the yaw profile is computed on ground, it is generated using predicted spacecraft positions rather than the actual positions. As a result, potential knowledge errors on the spacecraft positions may affect the cross-track placement of the footprints, since the yaw rotation will only correctly position them if the actual spacecraft positions match the propagated ones. To assess the impact of such knowledge errors on the footprint cross-track placement, perturbations were introduced into the simulated spacecraft positions.

The article is organized as follows. Section 2 provides a more in-depth description of the pointing problem and the mission constraints and requirements. Section 3 presents the numerical search strategy used to achieve the pointing of the ground path, while Section 4 outlines the numerical approach to achieve the alignment of radar footprints. The analytical formulation for the footprint-alignment problem, as well as the technical obstacles encountered in obtaining a closed-form solution, are discussed in Appendix A. Appendix B describes the equations required to define the local osculating-sphere approximation of the Earth's ellipsoid, which was adopted to locate the footprints on the Earth's surface. Section 5 presents the simulation of the pointing profiles for a single spacecraft in the constellation, as well as their variations under changes in orbital altitude or inclination. The effects of in-track knowledge position errors on both single-satellite and multi-satellite observations are also discussed in Section 5. Final remarks are provided in Section 6.

## 2. Problem formulation

The INCUS mission consists of a constellation of three smallsats, named INCUS 1, INCUS 2 and INCUS 3, flying on the same inertial orbital plane. According to the mission plan, the three spacecraft are to be released by the same launch vehicle on a common circular orbit. The entire system is expected to operate anywhere between 450 km and 580 km, with a range of possible inclinations being acceptable. For this analysis, we assume a mean altitude of 500 km and inclination of 38 degrees . The first spacecraft (INCUS 1) is notionally 30 s ahead of the second spacecraft (INCUS 2) and 120 s ahead of the third one (INCUS 3). This configuration derives from the scientific requirement that the constellation must observe the same 3-D profiles of radar reflectivity with a nominal time separation of 30, 90 and 120 s between each observation.

### 2.1. Ground-path pointing

To achieve time-differenced observations of the same 3-D reflectivity profiles, the three spacecraft are commanded to follow a common path on Earth. Since the spacecraft are released on the same inertial plane with an in-track time offset, their ground tracks shift relative to one another due to Earth's rotation. As a result, off-nadir pointing is required to align them with a common reference path. In particular, the reference path is defined as the ground track traced by a virtual spacecraft positioned 60 s behind INCUS 1, and thus 30 s behind INCUS 2 and 60 s ahead of INCUS 3. This choice minimizes the maximum off-nadir angle among the three spacecraft, and thus the parallax error among time-differenced observations of 3-D reflectivity profiles. Ideally, the nominal time separation between observations can be achieved by pointing each spacecraft to the intersection between the parallel passing through the subsatellite point and the reference ground path. However, the pointing strategy is subject to other scientific and instrumental constraints:

1. In order to minimize the parallax error among time-differenced observations of 3-D reflectivity profiles, it is required for the off-nadir angle of each spacecraft to be smaller than 5°;
2. In order to avoid strong surface clutter in the signal from specular returns from bodies of water, it is desirable to point at least one full beamwidth away from geodetic nadir.

For these reasons, each spacecraft is commanded to maintain a fixed forward pointing of 2.5° followed by a roll rotation to point to the common reference ground path. Consequently, the time separation between observations will differ from the in-track time separation between spacecraft [12]. The in-track time separation would then be adjusted such that the pointed spacecraft achieve the desired −60, −30, or +60 second observation time offset relative to the reference ground path.

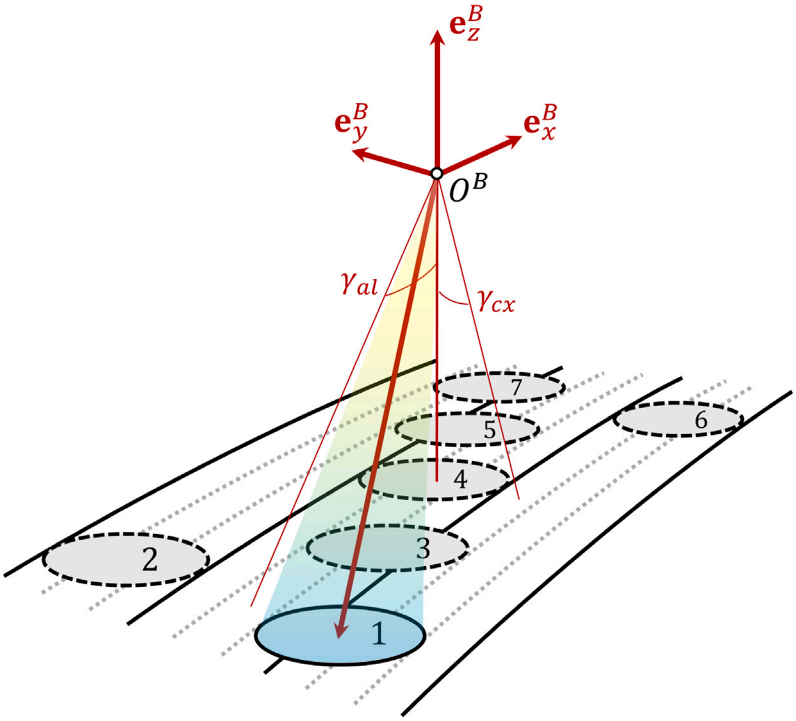

**Fig. 1.** Instantaneous 3 dB footprint pattern. The figure shows the time instant when only feed 1 is active. The other footprints (with dashed contours) serve as an illustration of the instantaneous footprint pattern if all the feeds were activated simultaneously.

### *2.2. Footprint pattern*

The Dynamic Atmospheric Radar (DAR) employed on each spacecraft consists of seven antenna feeds arranged to have adjacent 3 dB footprints overlapped by 2/3 across track. Fig. 1 provides a schematic representation of the instantaneous 3 dB footprint pattern of the DAR. Each feed is activated in sequence, one at a time, generating a beam whose boresight is assumed to be fixed relative to a spacecraft body-fixed reference frame. Denoting this frame as $F^B \triangleq \{O^B, \mathbf{e}^B\}$, where $O^B$ is a fixed point on the spacecraft and $\mathbf{e}^B$ a basis of axes rigidly attached to it, the boresight of each beam is defined by assigning the fixed angles $\gamma_{al}$ and $\gamma_{cx}$ relative to $F^B$. By choice, these two angles are set to zero for beam 4, which means that the latter is aligned with the $z$-axis of $F^B$.

Achieving the ideal footprint pattern shown in Fig. 1 is not straightforward, as the realization of the intended cross-track overlap depends on the spacecraft's orientation. Therefore, in addition to pitch and roll rotations required to point each spacecraft towards the reference ground path, an additional rotation is performed to yaw the spacecraft and ensure the footprints are aligned. The description and solution to this issue will be discussed in Section 4.

### *2.3. Knowledge position errors*

According to INCUS operations [13], each spacecraft has three ground contacts per day, which can be used to downlink the spacecraft position or uplink the pointing profiles. The pointing profiles, when generated on ground, would require the most recent spacecraft position to ensure accuracy. In particular, the pointing profiles would be generated using the downlinked spacecraft position from a given contact to generate the pointing profiles to uplink on the next contact. Given the asymmetry between contacts, the maximum time between contacts can be as large as 19 h, without accounting for potential missed contacts. A conservative approach would be then to consider the pointing profiles valid for two days. During this time, the spacecraft position is affected by knowledge errors that can be as large as 2 km and mostly affect the in-track direction. Indeed, a ±2 km error has been identified as a substantial along-track positional uncertainty over a two-day period under off-nominal conditions.

As the pitch, roll, and yaw profiles would be generated based on propagated spacecraft positions, any displacement of the latter introduce pointing errors. Specifically, if the pitch and roll profiles remain the same but are applied to spacecraft positions different from those used for their generation, then the spacecraft may no longer point towards the reference ground path. To overcome this issue, the spacecraft is commanded to track specific aimpoints uplinked from the ground station, instead of pitch and roll profiles. In the case of knowledge position errors, the spacecraft will still point towards the desired location, but with variations of the pitch and roll angles. On the other hand, the yaw profile is still generated on ground and uplinked during a convenient contact opportunity, as the spacecraft is assumed to lack the capability to generate it in real-time. The presence of knowledge errors on the propagated spacecraft positions may cause additional errors in the cross-track position of the footprints. These aspects are discussed in Section 5.

## 3. Ground-path pointing

The pointing strategy of INCUS consists in selecting and orienting a fixed axis of interest on the spacecraft (e.g., a boresight direction) towards the reference ground path. Without loss of generality, let the body-fixed axis $\mathbf{e}_z^B$ be the pointing direction. As shown in Fig. 1, this axis represents the $z$-axis of the body-fixed frame $F^B$, and coincides with the boresight of beam 4. The objective is to orient frame $F^B$ so that the designated pointing axis intersects the reference ground path. The orientation of $F^B$ is described relative to a Local-Vertical Local-Horizontal frame $F^L \triangleq \{O^B, \mathbf{e}^L\}$, whose axes are defined as follows:

$$\begin{aligned}
\mathbf{e}_x^L &\triangleq \mathbf{e}_y^L \times \mathbf{e}_z^L \\
\mathbf{e}_y^L &\triangleq \frac{\mathbf{r}_{IB} \times \mathbf{v}_{IB}}{\left\|\mathbf{r}_{IB} \times \mathbf{v}_{IB}\right\|} \\
\mathbf{e}_z^L &\triangleq \frac{\mathbf{r}_{IB}}{r_{IB}}
\end{aligned} \tag{1}$$

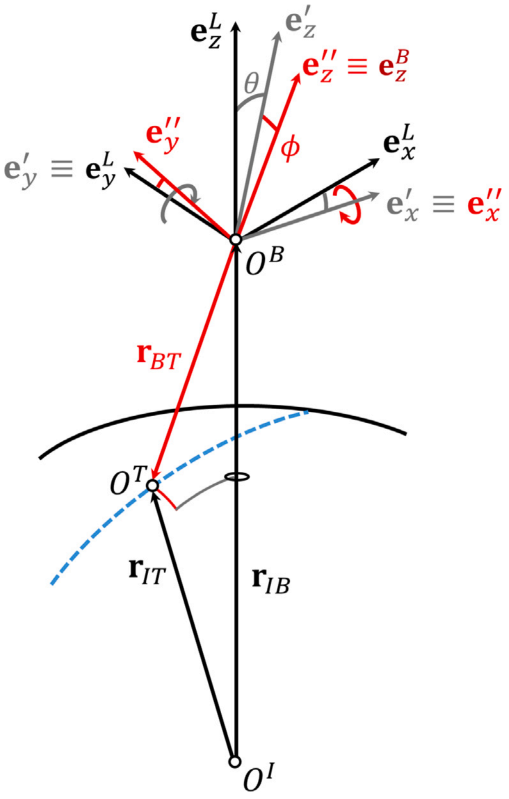

**Fig. 2.** Illustration of the ground-path pointing problem. The light blue dashed line represents the Earth-fixed ground path, while $O^T$ denotes the aimpoint observed on the path at a given time instant. $O^B$ is a point fixed with the spacecraft, while $O^I$ denotes the center of the Earth.

where $\mathbf{r}_{IB}$ and $\mathbf{v}_{IB}$ are the position and velocity of the spacecraft at time $t$, and $r_{IB} = \|\mathbf{r}_{IB}\|$. Note that $O^B$ has been set equal to the center of mass of the spacecraft, which is assumed to be a body-fixed point. The orientation of $F^B$ is described by a Y–X–Z sequence of rotations that superimposes frame $F^L$ onto frame $F^B$. As illustrated in Fig. 2, the first rotation is about axis $\mathbf{e}_y^L$ by angle $\theta$, named the pitch angle. Note that by the definition given for axis $\mathbf{e}_y^L$, positive pitch angles result in the DAR pointing backward. Consequently, forward-pointing of the DAR is achieved with negative pitch angles. This first rotation generates a reference frame $F' \triangleq \{O^B, \mathbf{e}'\}$. The second rotation is about axis $\mathbf{e}_x'$ by angle $\phi$, named the roll angle, which generates a second reference frame $F'' \triangleq \{O^B, \mathbf{e}''\}$. Lastly, the third rotation occurs about axis $\mathbf{e}_z''$ by angle $\psi$, named the yaw angle. As far as ground-path pointing is concerned, only the pitch and roll angles $\theta$ and $\phi$ need to be defined. The goal of the pointing problem can be summarized as finding the pitch and roll angles such that the pointing vector $\mathbf{r}_{BT}$, parallel to $\mathbf{e}_z^B$, aims at the reference ground path. Since the pitch angle $\theta$ is fixed due to mission constraints, the problem reduces to the computation of the roll angle $\phi$.

The first rotation of $\theta$ about $\mathbf{e}_y^L$ generates the intermediate reference frame $F'$. This frame is fully determined since frame $F^L$ is defined from the orbit and the value of $\theta$ is specified. Since the pointing vector $\mathbf{r}_{BT}$ is determined through the rotation of the unknown roll angle $\phi$ about $\mathbf{e}_x'$, vectors $\mathbf{r}_{BT}$ and $\mathbf{e}_x'$ must be orthogonal. Since the ground path is known as an interpolated function of a time series of Earth-fixed positions, the determination of the pointing vector can be formalized as the root-finding problem:

$$\mathbf{e}_x' \cdot \left[\mathbf{r}_{IG}(\tau) - \mathbf{r}_{IB}\right] = 0 \tag{2}$$

where $\mathbf{r}_{IG}(\tau)$ represents the ground path positions as a function of time. Finding the time instant $\tau^*$ for which the previous equation holds allows the computation of the pointing vector:

$$\mathbf{r}_{BT} = \mathbf{r}_{IT} - \mathbf{r}_{IB} \tag{3}$$

being $\mathbf{r}_{IT} \triangleq \mathbf{r}_{IG}(\tau^*)$ the position of the observed point $O^T$ on the reference ground path at time $t$. It is important to emphasize that two different time variables are being used. One is a time variable, denoted as $t$, related to the orbit propagation of the actual INCUS spacecraft. The other is a time variable, denoted as $\tau$, which describes the motion of the virtual spacecraft and its ground track positions. The pointing vector $\mathbf{r}_{BT}$, found at each time instant $t$, points to a unique point $O^T$ characterized by a specific time $\tau^*(t)$. Since this time represents the moment when the virtual spacecraft passed through the location identified by $O^T$, the time difference between observations is simply computed as:

$$\Delta t_{obs} = t - \tau^*(t) \tag{4}$$

Lastly, the roll angle is computed using geometric relationships between the axes of frames $F'$ and $F''$. The axes of $F''$ are defined based on the known axes of $F'$ and the pointing vector $\mathbf{r}_{BT}$ as follows:

$$\begin{aligned} \mathbf{e}_x'' &\equiv \mathbf{e}_x' \\ \mathbf{e}_y'' &\triangleq \mathbf{e}_z'' \times \mathbf{e}_x'' \\ \mathbf{e}_z'' &\triangleq -\frac{\mathbf{r}_{BT}}{r_{BT}} \end{aligned} \tag{5}$$

Noting that $\mathbf{e}_z'$ lies in both the plane defined by $\mathbf{e}_x^L$ and $\mathbf{e}_z^L$ and the plane defined by $\mathbf{e}_y''$ and $\mathbf{e}_z''$, the pitch and roll angles are given by:

$$\theta = \operatorname{atan2}\left(\mathbf{e}_z' \cdot \mathbf{e}_x^L, \mathbf{e}_z' \cdot \mathbf{e}_z^L\right) \tag{6}$$

$$\phi = \operatorname{atan2}\left(\mathbf{e}_z' \cdot \mathbf{e}_y'', \mathbf{e}_z' \cdot \mathbf{e}_z''\right) \tag{7}$$

Although Eq. (6) is clearly not needed at this stage (since the pitch angle $\theta$ is fixed) it will be of use for deriving the new pitch angles when knowledge errors on the spacecraft positions are considered (as described at the beginning of Section 5).

## 4. Footprint alignment

The measurement technique of INCUS requires the DAR of each spacecraft to observe a common ground path, with the swath characterized by footprints overlapping by 2/3 across track (Fig. 1). Although the antenna feeds are mounted to generate the intended footprint pattern, the actual footprint disposition around the reference ground path may differ. The actual footprint disposition primarily depends on the attitude of the spacecraft. Although pitch and roll rotations allow for tracking of the reference ground path, they do not account for the cross-track placement of the footprints relative to it and also introduce distortions on the footprint pattern. Fig. 3 illustrates the problem from an Earth-fixed perspective. As shown in the figure, footprint 6 is not aligned correctly after the pitch and roll rotations, as the footprint should be placed on the right track of the three-footprint-wide reference swath (in light blue). In general, the imprinted footprint at a particular time does not have the correct cross-track placement relative to the reference swath. The correction for the footprint misalignment can be achieved through a third attitude rotation. After defining the pitch and roll angles to achieve the ground-path pointing, the third degree of freedom around $\mathbf{e}_z''$ can be exploited to bring each footprint on the correct track (Fig. 3). Since by choice $\mathbf{e}_z''$ is defined as parallel to the pointing vector $\mathbf{r}_{BT}$, the rotation leaves the direction of the latter unchanged, while altering the boresight direction associated with the imprinted footprint, and thus its location relative to the reference ground path. The yaw angle $\psi$ needed to achieve this correction is derived through a numerical search strategy from an Earth-fixed perspective. An additional analytical formulation of the problem was undertaken to find a closed-form solution for the yaw rotation. The analysis was conducted from an inertial perspective, which enables

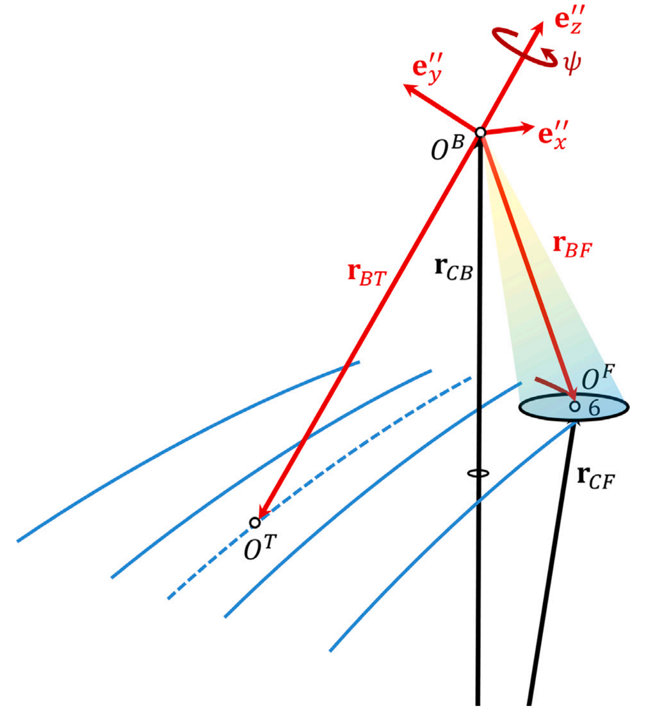

**Fig. 3.** Illustration of the footprint misalignment. The Earth-fixed reference swath is depicted in light blue, while the light blue dashed line in the middle represents the reference ground path. Imprinted footprint 6, taken here as an example, is depicted in black. Point $O^T$ represents the aimpoint, while $O^F$ is the center of the imprinted footprint. Note that the positions of the spacecraft and the footprint are here referenced to the center of curvature of the surface, $O^C$, rather than the Earth's center $O^I$ (see discussion in Section 4.1 and Appendix B). (For interpretation of the references to color in this figure legend, the reader is referred to the web version of this article.)

the description of the footprint misalignment relative to the reference ground path as a displacement resulting from Earth's rotation. Although a closed-form solution is not readily attainable, the approach may be of interest and is detailed in Appendix A. The next section describes the numerical search from an Earth-fixed perspective, as it offers a more intuitive and broadly applicable solution.

### 4.1. Footprint position

To quantify the cross-track placement of the footprint, it is first necessary to compute its location. This location is computed as the intersection between the boresight direction (given by $\mathbf{u}_{BF} = \mathbf{r}_{BF}/r_{BF}$) of the beam associated with the footprint and the Earth's surface. The first step is to define the Earth's surface. By modeling the Earth as a WGS84 ellipsoid, the surface in the vicinity of the observed point $O^T$ can be approximated as an osculating sphere (see Appendix B). Knowing the Earth-centered Earth-fixed (ECEF) coordinates of the position vector $\mathbf{r}_{IT}$, the surface normal at $O^T$ can be determined through (B.2). From the surface normal, the radius of curvature $R_C$ and the position of the center of curvature relative to the Earth's center, $\mathbf{r}_{CI}$, can subsequently be obtained through Eqs. (B.5) and (B.6). Once the surface has been defined, the second step is to convert the boresight direction from its known coordinate representation in the spacecraft's body frame to ECEF coordinates. Given that the spacecraft is considered oriented as frame $F''$ prior to the yaw rotation, the coordinate transformation is obtained through the direction cosine matrix from frame $F''$ to the ECEF frame at the time of observation.

The location of the footprint relative to the center of curvature (i.e., $\mathbf{r}_{CF}$) is determined through trigonometric considerations applied to the triangle formed by vectors $\mathbf{r}_{CB}$, $\mathbf{r}_{BF}$ and $\mathbf{r}_{CF}$, shown in Fig. 3. Given that the spacecraft's position vector $\mathbf{r}_{CB} = \mathbf{r}_{CI} + \mathbf{r}_{IB}$ and the boresight direction $\mathbf{u}_{BF}$ are known, and assuming that the magnitude of $\mathbf{r}_{CF}$ is equal to the radius of curvature $R_C$ based on a locally spherical Earth assumption, it is possible to use the laws of sines to write:

$$\frac{\sin\left(\pi - \eta_F\right)}{r_{CB}} = \frac{\sin \eta_B}{r_{CF}} \tag{8}$$

where $\eta_F$ is the unknown interior angle between $\mathbf{r}_{BF}$ and $\mathbf{r}_{CF}$, and $\eta_B$ is the known interior angle between $\mathbf{r}_{CB}$ and $\mathbf{r}_{BF}$. By solving (8) for $\eta_F$, the interior angle between $\mathbf{r}_{CB}$ and $\mathbf{r}_{CF}$ is computed as $\eta_C = \pi - (\eta_F + \eta_B)$. By using basic trigonometry, the magnitude of $\mathbf{r}_{BF}$ can be computed as:

$$r_{BF} = \frac{r_{CB} - r_{CF}\cos \eta_C}{\cos \eta_B} \tag{9}$$

Knowing both the direction and magnitude of $\mathbf{r}_{BF}$, the footprint position can be computed as $\mathbf{r}_{CF} = \mathbf{r}_{CB} + \mathbf{r}_{BF}$, where all vectors are expressed in ECEF coordinates.

### 4.2. Footprint cross-track angle

Once the position of the footprint is known, its cross-track angle relative to the reference ground path can be computed. The first step is to define a reference frame along the ground path that defines the along-track and cross-track directions. To this end, both positions and velocities of the ground path are required. Given that the reference ground path is assumed to be a known time series of ECEF positions, its velocity can be estimated numerically. A reference frame $F^G \triangleq \left\{O^G, \mathbf{e}^G\right\}$ can be defined for each position $O^G$ as:

$$\begin{aligned}
\mathbf{e}^G_x &\triangleq \mathbf{e}^G_y \times \mathbf{e}^G_z \\
\mathbf{e}^G_y &\triangleq \frac{\mathbf{u}_n \times \mathbf{v}^e_{IG}}{\left\|\mathbf{u}_n \times \mathbf{v}^e_{IG}\right\|} \\
\mathbf{e}^G_z &\triangleq \mathbf{u}_n
\end{aligned} \tag{10}$$

being $\mathbf{u}_n$ the unit surface normal at $O^G$ and $\mathbf{v}^e_{IG}$ the earth-fixed velocity of the reference ground path, expressed in ECEF coordinates. The cross-track angle is measured at the point on the reference ground path where the footprint is perpendicular. By interpolating the along-track unit vector $\mathbf{e}^G_x$ along the ground path, this condition can be formulated as the root-finding problem:

$$\mathbf{e}^F_z \cdot \mathbf{e}^G_x(\tau) = 0 \tag{11}$$

where $\mathbf{e}^F_z \triangleq \mathbf{r}_{CF}/r_{CF}$ and $\tau$ is the time variable related to the virtual spacecraft propagation. The interpolated axes of frame $\mathbf{e}^G$ are then evaluated at the root, from which the cross-track angle $\epsilon$ can be computed as:

$$\epsilon = \operatorname{atan2}\left(\mathbf{e}^F_z \cdot \mathbf{e}^G_y, \mathbf{e}^F_z \cdot \mathbf{e}^G_z\right) \tag{12}$$

### 4.3. Footprint relocation

The position of the footprint is modified via a yaw rotation so that its cross-track angle relative to the reference ground path matches the desired value $\epsilon_d$. The desired cross-track angle $\epsilon_d$ is computed by assigning an ideal orientation and beam configuration to the virtual spacecraft. In particular, the virtual spacecraft is assumed to have its $z$-axis pointed at the geodetic nadir, with its $x$-axis aligned with the ground track earth-fixed velocity at its subsatellite point. The beam configuration of the virtual spacecraft shares the same $\gamma_{cx}$ angles (illustrated in Fig. 1) as the actual INCUS spacecraft, but the angles $\gamma_{al}$ in the forward-aft direction are set to zero. The cross-track angles of the footprints generated by the virtual spacecraft set the reference for the relocation algorithm. The algorithm consists of the following iterative procedure, illustrated in Fig. 4:

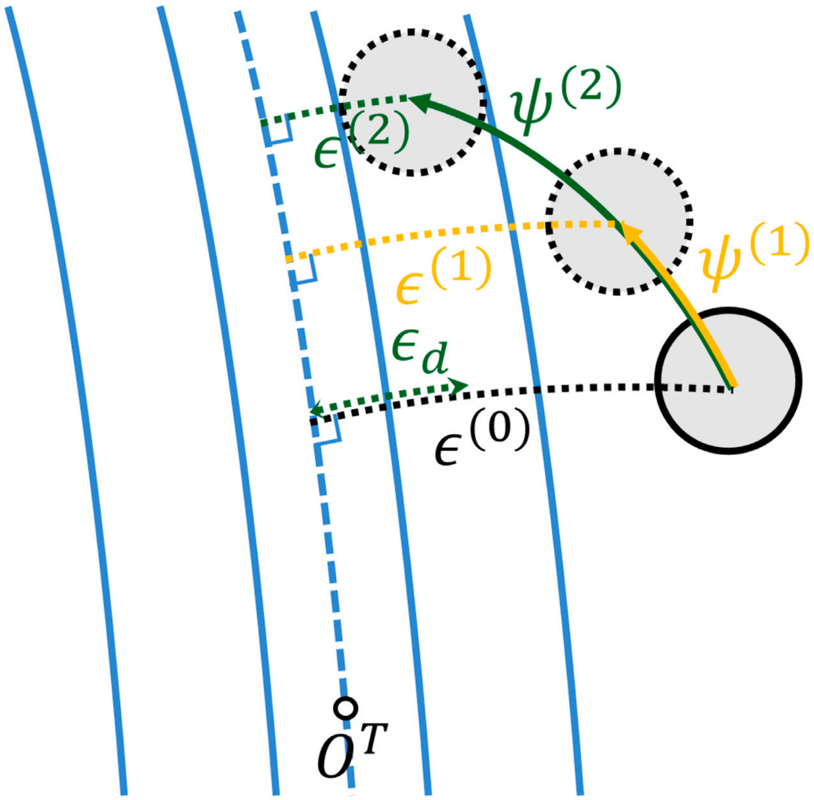

**Fig. 4.** Footprint's relocation strategy. $\epsilon^{(0)}$ represents the cross-track angle prior to the yaw rotation, while $\epsilon^{(1)}$ and $\epsilon^{(2)}$ correspond to the values resulting from the tentative yaw rotations $\psi^{(1)}$ and $\psi^{(2)}$, respectively.

1. A tentative yaw angle $\psi$ is applied. The boresight direction of the footprint is rotated around $\mathbf{e}_z''$ by $\psi$ (see Fig. 5):

   $$\mathbf{u}_{BF}^c = \mathbf{T}\left(\psi, \mathbf{e}_z''\right) \cdot \mathbf{u}_{BF} \tag{13}$$

   where:

   $$\mathbf{T}(\vartheta, \mathbf{u}) = \mathbf{E} + \tilde{\mathbf{u}} \sin\vartheta + 2\tilde{\mathbf{u}}\tilde{\mathbf{u}} \sin^2\frac{\vartheta}{2} \tag{14}$$

   is the general Rodriguez formula for the rotation dyadic [14, Section 2.1], in which $\vartheta$ and $\mathbf{u}$ are the angle and axis of rotation, while $\mathbf{E}$ is the 3 × 3 identity dyadic and $\tilde{\mathbf{u}}$ the 3 × 3 skew-symmetric dyadic of $\mathbf{u}$.
2. The new geocentric position of the footprint, $\mathbf{r}_{CF}^c$, is computed following the procedure described in Section 4.1, through which $\mathbf{r}_{CF}^c$ is found knowing the spacecraft position, $\mathbf{r}_{CB}$, the rotated boresight direction of the footprint, $\mathbf{u}_{BF}^c$, and the radius of the osculating sphere, $R_C$, at point $O^T$.
3. The cross-track angle $\epsilon$ associated with the new position of the footprint is evaluated through Eq. (12) after solving the root-finding problem (11).
4. Steps 1 to 3 are repeated until the condition $\epsilon = \epsilon_d$ is met.

## 5. Results

The methodology described in Sections 3 and 4 is applied to the nominal INCUS orbital configuration (Table 1) to generate the spacecraft pointing profiles (Section 5.1). INCUS 1, 2, and 3 share the same orbit as the virtual spacecraft, but they are spaced relative to it by an in-track time separation of +60, +30 and −60 s, respectively. Although the pointing geometry relative to the common reference ground path — and therefore the pointing profiles — varies among the spacecraft because of their different in-track time separation, the attitude strategy used to generate these profiles is identical for all of them. For this reason, the simulation will focus on one particular spacecraft of the constellation. Since the off-nadir angles increase as the in-track time separation increases, INCUS 1 was selected as a case study, as it exhibits the largest absolute in-track time separation relative to the virtual spacecraft, together with INCUS 3. In what follows, the virtual spacecraft is set as pointed at its geodetic nadir, with its $x$-axis aligned with the ground track earth-fixed velocity at its subsatellite point. INCUS 1 is commanded to point towards the ground track of the virtual spacecraft through a sequential pitch and roll rotations. Since the pitch is set equal to −2.5° (forward pointing), only the roll profile is presented. The time difference between observations associated with this pointing strategy is also presented.

**Table 1**
Orbital elements.

| | |
|---|---|
| Epoch | June 1st 2026 |
| Semi-major axis | 6878 km |
| Inclination | 38 deg |
| Eccentricity | 0 |
| Argument of perigee | 0 deg |
| Longitude of node | 0 deg |

The radar employed by INCUS 1 generates seven sequentially activated beams. The boresight associated with each beam is considered fixed relative to the body-fixed frame $F^B$, with orientation described by a pair of angles $\gamma_{al}$ and $\gamma_{cx}$, as illustrated in Fig. 1. The values for $\gamma_{al}$ and $\gamma_{cx}$ are provided in Table 2. The same $\gamma_{cx}$ angles are considered for the beam configuration of the virtual spacecraft, but with angles $\gamma_{al}$ set to zero. The yaw profile associated with the beam configuration of Table 2 is presented for INCUS 1. The effectiveness of the yaw rotation is then evaluated in terms of cross-track distance of the footprints relative to the reference ground path.

Additional simulations are presented in Section 5.2 to assess how knowledge errors on the spacecraft position affect the pointing profiles

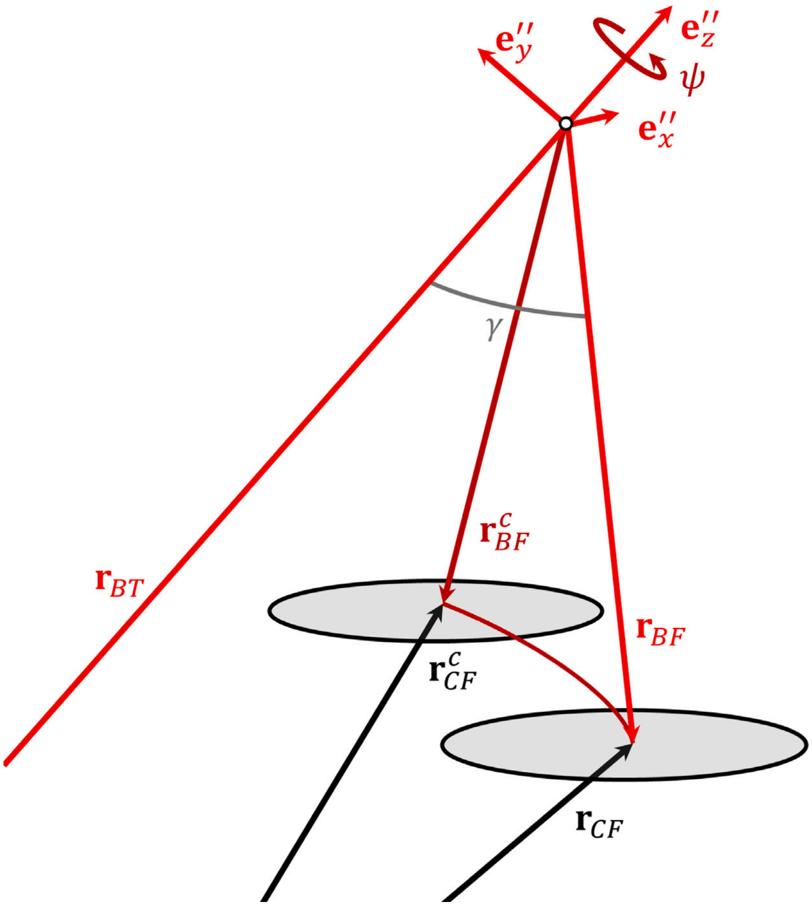

**Fig. 5.** Illustration of the footprint relocation through a yaw rotation.

**Table 2**
Angles describing the orientation of each beam's boresight relative to body frame $F^B$. The beams numbering denotes the order of activation.

| | $\gamma_{al}$ [deg] | $\gamma_{cx}$ [deg] |
|---|---|---|
| Beam 1 | −1.2 | −0.2333 |
| Beam 2 | −1 | 0.35 |
| Beam 3 | −0.6 | −0.1167 |
| Beam 4 | 0 | 0 |
| Beam 5 | 0.6 | 0.1167 |
| Beam 6 | 1 | −0.35 |
| Beam 7 | 1.2 | 0.2333 |

and the cross-track distance of the footprints. Following the considerations in Section 2.3, the spacecraft is pointed towards the same aimpoints derived for the nominal case, but its position at the time of observation is modified to simulate the knowledge position error. This results in a variation of the pointing vector $\mathbf{r}_{BT}$, along with frames $F^L$ and $F''$. The pitch and roll angles corresponding to the new spacecraft's position and attitude are then simulated. The yaw profile is kept the same as in the nominal case, but it is now referenced to the $z$-axis of the new $F''$ frame. As this modifies the cross-track placement of the footprints relative to the reference ground path, the cross-track distances are simulated again for the new spacecraft's position and attitude. The spacecraft's position error is introduced by rotating the spacecraft's position vector $\mathbf{r}_{IB}$ around the instantaneous direction of the orbital angular momentum. The rotation angle is computed as $l/r_{IB}$, being $l$ the arc displacement associated with the knowledge position error. First, the pointing profiles are simulated for $l = 2\,\text{km}$, which is representative of a significant along-track knowledge position error in off-nominal scenarios. Then, a sensitivity analysis for $l = -2, -1.9, \ldots, 2\,\text{km}$ is carried out to evaluate the cross-track errors of the footprints, relative to their desired value, for different position errors on the spacecraft position. An additional sensitivity analysis was conducted for multi-satellite observations to assess the relative cross-track distance between footprints imprinted by different spacecraft of the constellation under different combinations of the knowledge position error. Finally, Section 5.3 illustrates the effects of variations in the orbital average altitude and inclination on the pointing profiles and provides a verification of the 2/3 footprint-overlap requirement under these variations.

The simulation is run for a single orbital period, with a time step of 20 ms corresponding to the sequential activation of the antenna feeds. The orbit and the ground track were simulated using the Python library Skyfield [15], which implements the SGP4 model for the orbit and the WGS84 model for the Earth. The code was implemented in Python.

### 5.1. Nominal case

This section presents the results corresponding to the orbital parameters in Table 1, the beam configuration in Table 2, and considering a fixed-pitch pointing strategy. A representation of the pointing strategy from a ground track perspective is provided in Fig. 6. The figure shows the subsatellite point of INCUS 1 (red dot) when the argument of latitude $u$ is equal to 45°. For a fixed forward pitch pointing of 2.5°, INCUS 1 intercepts the ground track of the virtual spacecraft at point $O^T$. Given the time of observation of INCUS 1, the subsatellite point of the virtual spacecraft after 60 s (i.e., the in-track time separation) is represented for reference by a hollow circle. As this point and $O^T$ are observed at different times from the virtual spacecraft, a direct implication is that the pointing strategy changes the difference between

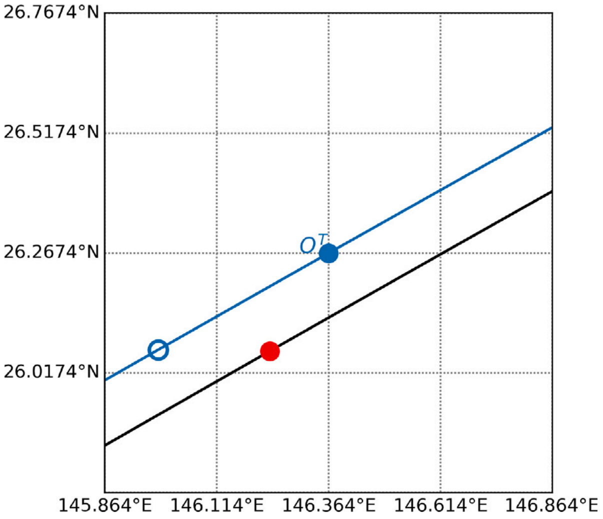

**Fig. 6.** Ground track of the virtual spacecraft (in blue) and INCUS 1 (in black). The observed point is $O^T$, while the red point represents the subsatellite point of INCUS 1 when its argument of latitude is 45°. The hollow blue circle represents the point on the reference ground path where the time difference between observations is equal to 60 s. (For interpretation of the references to color in this figure legend, the reader is referred to the web version of this article.)

the observation time of INCUS 1 and the observation time of the virtual spacecraft. Fig. 7 shows the time difference between observations, as defined in (4). The time difference is negative because INCUS 1 is ahead of the virtual spacecraft, meaning that a given point is observed earlier from INCUS 1. As shown in the figure, the pointing strategy increases the time difference between observations by approximately 6.5 s compared to the nominal in-track time separation. The variation of $\Delta t_{obs}$ along the orbit is caused by effects of a non-zero osculating eccentricity, which introduces a variation at the orbital frequency, and the change in the geocentric radial distance of the observed points due to the Earth's oblateness, which leads to a more significant variation at twice the orbital frequency.

Fig. 8 illustrates the time series of the roll angle required to point towards the reference ground path. As shown, the roll time series is well approximated by a cosine function with orbital frequency and with amplitude of approximately 2.2°. Maximum roll values occur near the equator, where the shift between the ground tracks is the greatest. Zero roll angles occur slightly before the argument of latitude of INCUS 1 reaches 90° and 270°. Specifically, zero roll values occur when INCUS 1, considered as tilted solely by the fixed-pitch angle relative to frame $F^L$, has pointing vector $\mathbf{r}_{BT}$ intersecting the reference ground path. For a given orbit and in-track time separation, the argument of latitude of INCUS 1 where this occurs depends on the value of the fixed-pitch angle and the Earth model used to define the reference ground path. Indeed, the argument of latitude at the zero-roll crossing has been observed to change when a spherical Earth model is used instead of the WGS84 ellipsoid to define the reference ground path.

The time series of the yaw angle is illustrated in Fig. 9. The unfiltered time series (in blue) exhibits high-frequency oscillations, which reflect small unsmooth variations of the yaw angle when moving from one footprint to another. In fact, these oscillations result from the footprint arrangement on ground and the corresponding change in geometry when passing from one to another. The distortions in the footprint pattern introduced by the roll angle are the main source of these perturbations, as they are more evident where the roll values are higher. There is also an additional effect caused by the non-planarity of the reference ground path, but it does not appear to be significant. While the unfiltered time series represents the yaw values that achieve the correct footprint alignment, its high-frequency variations are undesirable for the spacecraft. For this reason, since the oscillations repeat after the same beam is activated, they are smoothed out by performing a moving average with a number of samples that is an integer multiple of the number of beams. In the presented simulation, a Savitzky–Golay filter with 70 samples has been used. The averaged time series is shown in orange, and almost completely overlaps with the fitted cosine function. Similar to the roll profile, the yaw profile exhibits orbital periodicity with an amplitude of about 2.53°. Maximum yaw angles are observed near the equator, where footprints exhibit the largest out-of-track velocity components relative to the inertial subsatellite trajectory of the virtual spacecraft (see Appendix A and Fig. 19). Zero yaw values are expected when INCUS 1 points near the highest and lowest latitudes of the reference ground path, as in this case the footprint velocity would have zero out-of-track component. Additional variability on the location of the zero-yaw crossing is introduced by the values set for the reference cross-track angles $\epsilon_d$, and by the pitch and roll angles, as the initial uncorrected position of the footprint influence the entity of the yaw rotation.

Fig. 10 illustrates the footprints' cross-track distance after the yaw rotation, and the corresponding desired reference values. Small differences are observed between the cross-track positions of the footprints imprinted from INCUS 1 (solid green curve) and the reference ones (solid blue curve). Note that this error is caused by the yaw–averaging operation shown in Fig. 9, as the cross-track distance of the footprints matches the desired reference values when the unaveraged yaw (dotted green curve) is applied. The cross-track distances exhibit overall variations over time, which are a direct consequence of altitude variations (Fig. 11) resulting from both the orbit and the Earth's ellipsoidal model. The dashed orange curve represents the cross-track distance of the footprints in the case of a +2 km knowledge error on the spacecraft's position and is discussed in Section 5.2. By comparing the different subplots in Fig. 10, it can be observed that adjacent footprints exhibit a cross-track angular distance of approximately 1 km. Given that the footprint radius associated with the nominal INCUS configuration is about 3 km, the 2/3 overlap requirement is satisfied. On the other hand, the desired footprint overlap is not achieved when the corrective yaw rotation is not performed, as illustrated in Fig. 12. In the absence of yaw correction, the footprints are correctly placed only twice along the orbit (that is when the red and green curves intersect). This occurs when the yaw angle in Fig. 9 is zero.

### 5.2. Effects of knowledge position errors

Fig. 13 illustrates the new pitch profile associated with a forward in-track variation of the spacecraft's position of 2 km. The pitch angle, initially set to a fixed value of −2.5°, now exhibits variability along the orbit and shows smaller values overall. The smaller values result from moving the spacecraft position forward, which reduces the forward pitch required to point to the same aimpoint. The variability, on the other hand, is caused by changes in altitude, as can be seen by comparison with Fig. 11. Although the variation in pitch angle is not negligible, its absolute minimum value remains sufficiently large to prevent the occurrence of strong clutter returns that may happen when pointing nadir. Fig. 14 shows the comparison between the original roll angle and its profile in the case of a +2 km position error. The roll profile is marginally affected by the introduction of the in-track position error, as the two profiles are almost coincident.

As pointed out earlier, Fig. 10 shows the cross-track distance of the footprints in the case of a +2 km in-track knowledge error on the spacecraft's positions (in orange). Small differences with respect to the reference cross-track angles (solid blue curve) are observed when a +2 km position error is considered (dashed orange curve). Fig. 15 shows the maximum and mean of the absolute values of this difference for position errors ranging from −2 km to +2 km. It can be observed that the mean of the absolute error decreases for footprints

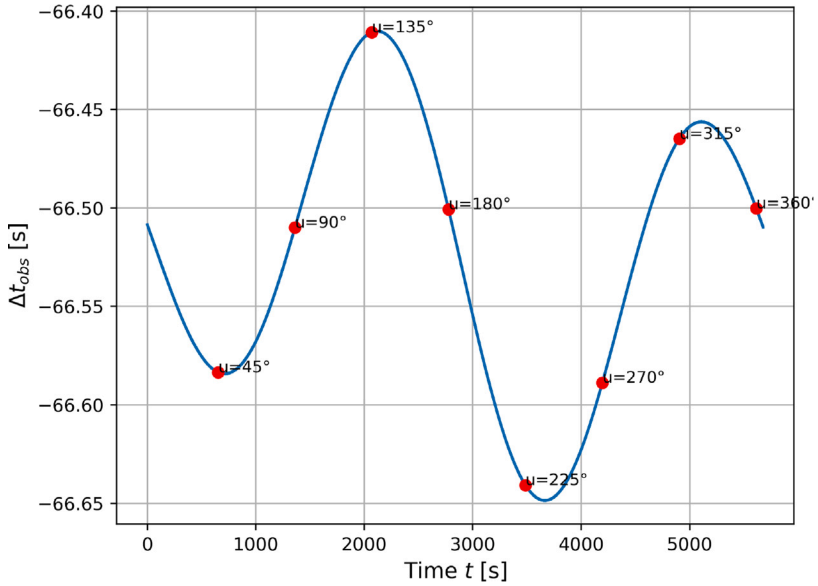

**Fig. 7.** Time difference between observations. The red dots highlight the time difference at specific arguments of latitude of INCUS 1.

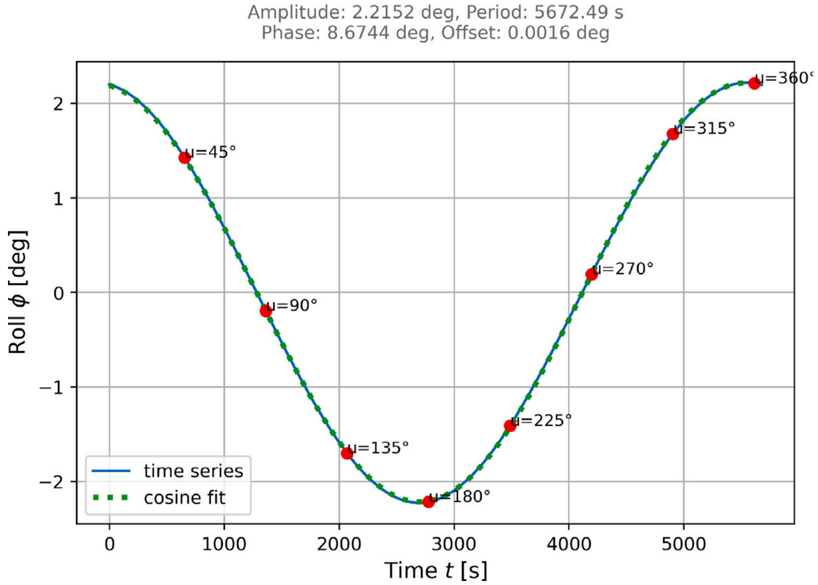

**Fig. 8.** Roll time series (in blue) and its cosine fit (green dashed). The top of the figure shows the parameters of the cosine function. The red dots highlight the values of the roll angle at specific arguments of latitude of INCUS 1.

2, 5, 6 and 7 moving from negative to positive knowledge position errors, indicating that the presence of positive position errors brings these footprints closer, on average, to the desired cross-track distance values. For footprints 1 and 3, a decrease is followed by an increase while moving from negative to positive knowledge position errors. Overall, it can be observed that the maximum absolute error among the footprints occurs for footprint 6, with a magnitude of approximately 15 m occuring for a knowledge position error of $-2$ km. The impact of this error on the scientific retrievals is negligible.

While Fig. 15 illustrates the impact of knowledge position errors on the footprints' cross-track distance relative to the desired values for INCUS 1, it does not account for the relative error between footprints when considering multi-satellite observations. Specifically, it is of interest to analyze the relative error in the cross-track distance at the same coordinate along the common reference ground path between a footprint imprinted by a spacecraft of the constellation and the same footprint (i.e, with the same label number) imprinted by another spacecraft. In visual and practical terms, this error is computed by generating the dashed orange curves in Fig. 10 for a given spacecraft and for different knowledge position errors, and then computing the difference with the corresponding curves generated for another spacecraft and for different knowledge position errors. It is important to recall that the orange curves generated for a given knowledge position error are affected not only by the knowledge position error itself but also by yaw averaging. Because two different spacecraft of the constellation might introduce different yaw-averaging-induced errors, these combine with those induced by the knowledge position error in the multi-satellite error analysis.

The cross-track errors of the footprints among multi-satellite observations were simulated for the combinations INCUS 1 – INCUS 2, INCUS 1 – INCUS 3, and INCUS 2 – INCUS 3. The maximum and mean

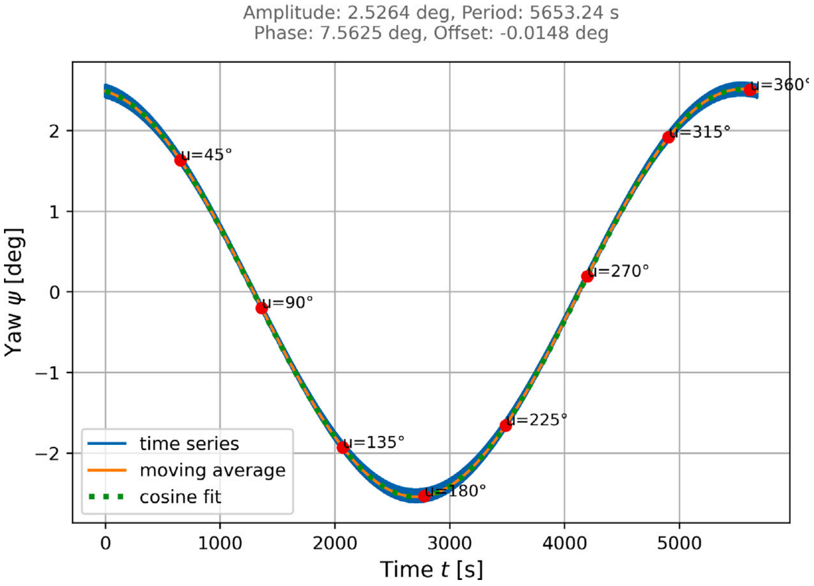

**Fig. 9.** Yaw time series (in blue), moving average (in orange) and cosine fit (green dashed). The top of the figure shows the parameters of the cosine function. The red dots highlight the yaw angle at specific arguments of latitude of INCUS 1. (For interpretation of the references to color in this figure legend, the reader is referred to the web version of this article.)

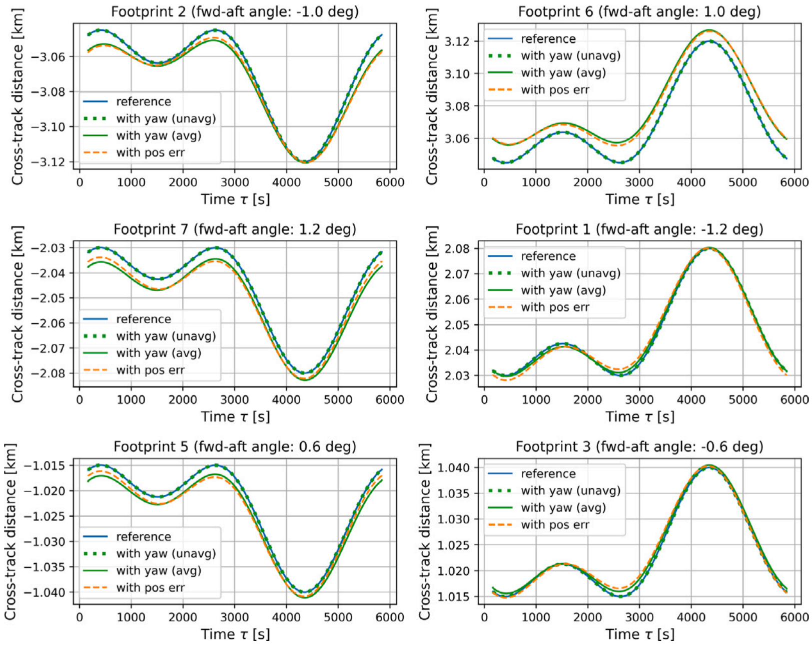

**Fig. 10.** Cross-track angular distance of the footprints relative to the reference ground path. Footprint 4 is omitted, as its center is designed to lie on the reference ground path. (For interpretation of the references to color in this figure legend, the reader is referred to the web version of this article.)

absolute cross-track errors for different combinations of knowledge position errors were then analyzed for each multi-satellite configuration. Fig. 16 shows the results for the INCUS 1 − INCUS 2 multi-satellite configuration, which was found to exhibit the largest error. As shown in Fig. 16, the largest maximum absolute error (top figure) and the largest mean absolute error (bottom figure) occur for footprint 6 for the knowledge position error combination (+2 km, −2 km), with values of approximately 8 m and 3.5 m, respectively. Lower values, both in the maximum absolute error and in the mean absolute error, are observed for the other footprints, with the largest values occurring for the two knowledge position error combinations (−2 km, +2 km) and (+2 km, −2 km). Given the magnitude of these errors, their impact on the scientific retrievals is negligible and does not affect the accuracy of the time-differenced radar observations.

### *5.3. Effects of altitude and inclination variations on roll and yaw profiles*

The roll and yaw profiles derived for the nominal orbit configuration are subject to variations when different inclinations or altitudes are considered. This section illustrates how the roll and yaw profiles change when considering a range of inclinations from 28° to 48° or altitudes from 450 km to 580 km, which are feasible for the INCUS constellation. As shown in Figs. 8 and 9, both the roll and yaw profiles are well approximated by a cosine function with specific amplitude and orbital

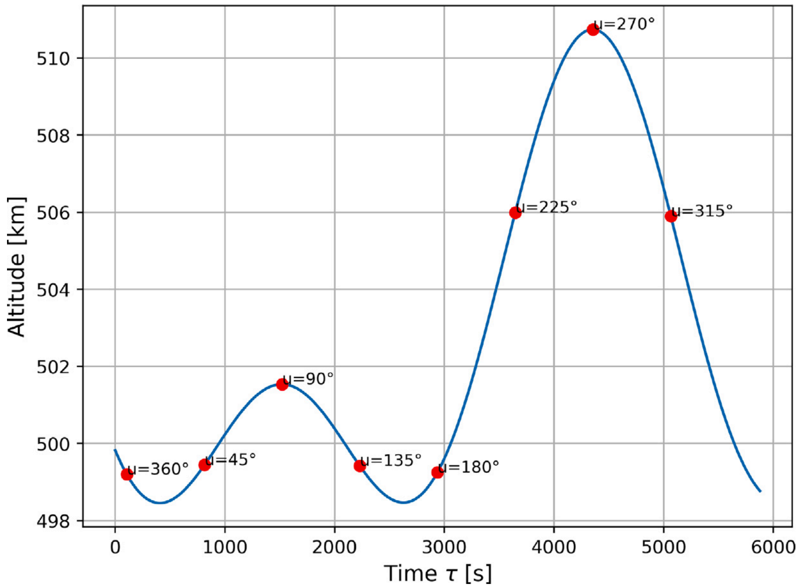

**Fig. 11.** Altitude of the virtual spacecraft. The red dots highlight the altitude at specific arguments of latitude of the virtual spacecraft.

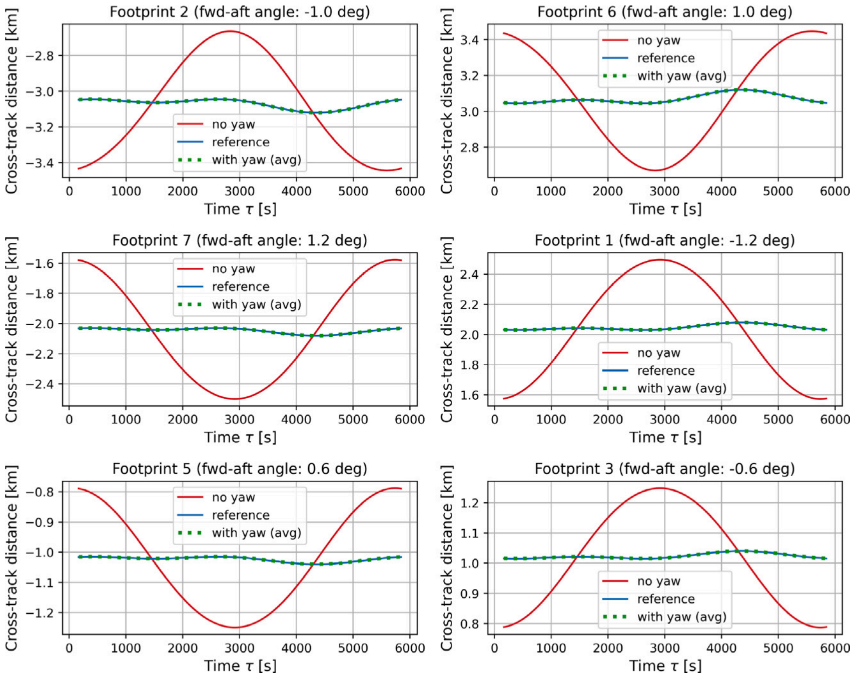

**Fig. 12.** Cross-track angular distance of the footprints relative to the reference ground path. Footprint 4 is omitted, as its center is designed to lie on the reference ground path. (For interpretation of the references to color in this figure legend, the reader is referred to the web version of this article.)

frequency. The amplitude of the roll and yaw profiles varies as the inclination or the average altitude of the orbit changes. The variation in the amplitude of the pointing profiles is analyzed for INCUS 1, taken here once again as an illustrative example.

Fig. 17(a) depicts the change in amplitude for the roll and yaw profiles as the average altitude varies from 450 to 580 km. While the semi-major axis is adjusted to achieve the altitude variation, the other orbital elements are kept the same as in Table 1. As shown, the roll amplitude decreases as the average altitude increases. Since the in-track time separation is fixed, the relative shift between the ground tracks is not affected by the increase in altitude. However, because of the greater altitude, smaller roll angles are required to cover a comparable distance on the ground. This explains the reduction in the roll amplitude as the average altitude increases. A second effect of the altitude increment is the decrease in orbital velocity, which in turn modifies the angle between the tangent to the reference ground path on the Earth and the East direction. Recall that the reference ground path corresponds to the ground track of the virtual spacecraft, which is also affected by the increase in altitude. For the considered orbital configuration, the variation of the reference ground path due to an increase in altitude causes the uncorrected footprint (i.e., the one that would be imprinted with zero yaw) to be placed, on average, farther from the desired cross-track distance. Consequently, a larger yaw is required to place the footprint correctly.

Fig. 17(b) depicts the change in amplitude for the roll and yaw profiles as the inclination varies from 28° to 48°, while the other

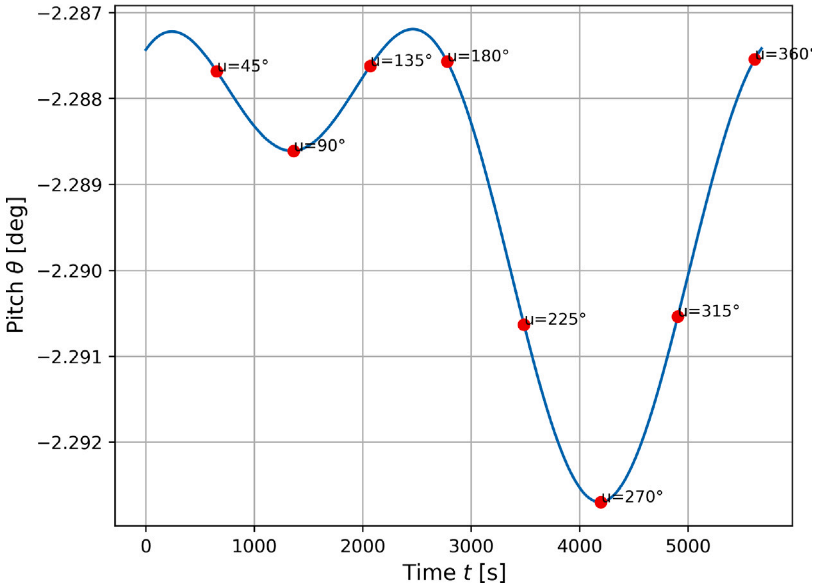

**Fig. 13.** Pitch profile for a forward in-track position error of 2 km. The red dots highlight the pitch angle at specific arguments of latitude of INCUS 1.

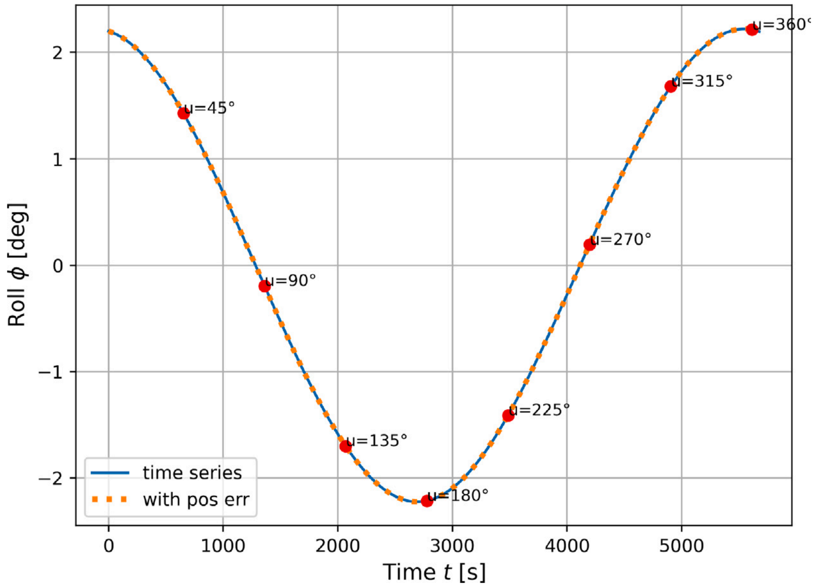

**Fig. 14.** Roll time series (in blue) and its profile in case of a forward in-track position error of 2 km (orange dashed). The red dots highlight the roll angle at specific arguments of latitude of INCUS 1.

orbital elements are kept the same as in Table 1. As shown, the roll amplitude increases as the inclination increases. This effect is due to a greater relative shift between the ground track of INCUS 1 and the virtual spacecraft occurring during the 60 s in-track time separation. An increase in yaw amplitude is also observed as the inclination increases. This effect follows from considerations similar to those made for the altitude case, as an increase in inclination modifies the angle between the tangent to the reference ground path on the Earth and the East direction.

Lastly, Fig. 18 shows the verification of the 2/3 footprint-overlap requirements in the case of variations in average altitude (Fig. 18(a)) or inclination (Fig. 18(b)). For each orbit, characterized by a given average altitude or inclination, the mean cross-track distance of each footprint relative to the reference ground path was computed. The mean footprint diameter (vertical red lines) was also calculated for each orbit, based on the central beam of the virtual spacecraft, which by design points towards its geodetic nadir. As can be visually observed, the 2/3-overlap requirement is always satisfied, since adjacent footprints have their centers separated by one-third of the total footprint diameter.

## 6. Conclusions

The present work describes the derivation of pointing profiles for a mission requiring continuous observation of a ground path. The study is specifically applied to the INCUS mission, which employs a constellation of three satellites to enable the systematic investigation of tropical convective storms. Mission-specific constraints and requirements were considered during the derivation of the pointing profiles. In particular, a fixed-pitch strategy was performed for ground-path pointing, while yaw maneuvering has been explored to achieve cross-track alignment of the footprints. A numerical search strategy was employed to derive both the roll and yaw profiles, and an additional analytical formulation is provided to address the footprint alignment problem. The methodology

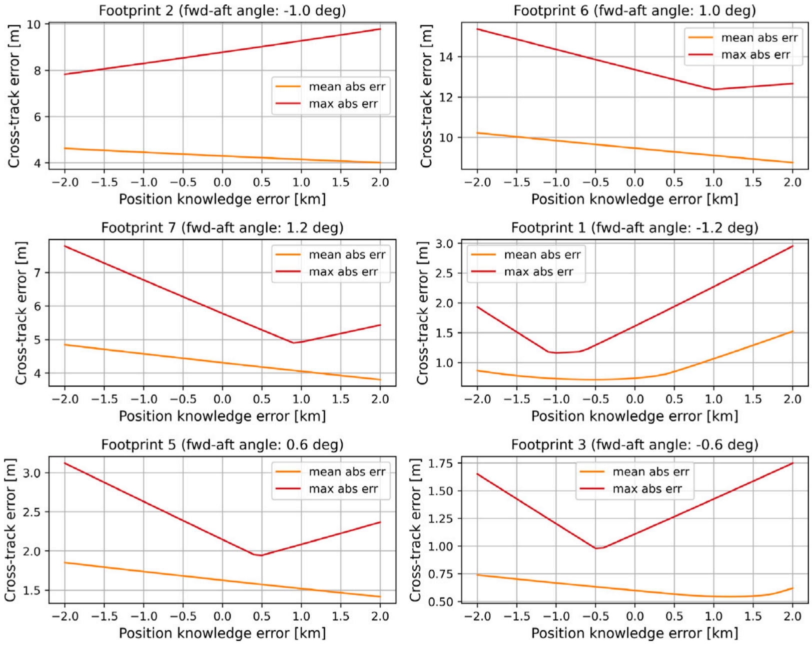

**Fig. 15.** Cross-track error of the footprints for different in-track knowledge position errors on the spacecraft positions. Footprint 4 is omitted, as its center is designed to lie on the reference ground path.

was first applied to a single-satellite simulation to generate and analyze the pointing profiles and verify the correct cross-track alignment of the footprint. A single-satellite simulation was also carried out to illustrate the variation in the amplitude of the pointing profiles with changes in average altitude or inclination, as well as to verify the 2/3 footprint-overlap requirement under these variations. The impact of spacecraft position-knowledge errors on the pointing profiles was analyzed for a single spacecraft, while their effect on the cross-track alignment of the footprints was analyzed for both single-satellite and multi-satellite observations.

Results from a single-orbit simulation of INCUS 1 show that both roll and yaw profiles exhibit a cosine-like pattern with orbital periodicity. An increase in the yaw amplitude was observed with increasing average altitude or inclination. In contrast, the roll amplitude decreased with increasing average altitude, while it increased with increasing inclination. For the considered range of average altitudes and inclinations, the angular values of the pointing profiles remain smaller than 3°. Given the symmetric orbital disposition of INCUS 1 and INCUS 3 relative to the virtual spacecraft, with INCUS 2 being closer to it, comparable or lower values of the pointing profiles are expected for the other two spacecraft of the constellation. Given the small angular values of the pointing profiles, the parallax error on time-differenced observations of 3-D reflectivity profiles is expected to remain within acceptable limits. The results also demonstrated that yaw rotation enables accurate cross-track alignment of the footprints with the desired overlap.

The single-satellite analysis showed negligible errors in the cross-track distances of the footprints relative to their desired values when position-knowledge errors were considered. The multi-satellite analysis showed that the relative error between multi-satellite observations is also negligible, and therefore does not affect the accuracy of the time-differenced radar measurements.

Lastly, the single-satellite simulation showed that the time interval between observations varies due to the pointing strategy; therefore, a modification of the in-track time separation between spacecraft is required to achieve the nominal time separations between observations of the same location on the ground.

## CRediT authorship contribution statement

**Paolo Martire:** Writing – original draft, Visualization, Validation, Software, Methodology, Investigation, Formal analysis, Conceptualization. **Quinn Kostelecky:** Writing – review & editing, Validation, Supervision, Conceptualization. **Kenza Boudad:** Writing – review & editing, Validation, Supervision, Conceptualization. **Simone Tanelli:** Writing – review & editing, Validation, Supervision, Resources, Project administration, Funding acquisition, Conceptualization. **Alessandro Battaglia:** Writing – review & editing, Supervision, Resources, Project administration, Funding acquisition.

## Declaration of competing interest

The authors declare that they have no known competing financial interests or personal relationships that could have appeared to influence the work reported in this paper.

## Acknowledgments

The work by Paolo Martire has been funded by the Italian Ministry of University and Research (MUR) as part of the PNRR-NGEU project (Ministerial Decree DM 351/2022).

The research was carried out at the Jet Propulsion Laboratory, California Institute of Technology, under a contract with the National Aeronautics and Space Administration, United States (80NM0018D0004).

## Appendix A

This section provides an analytical formulation of the footprint alignment described in Section 4 from an inertial perspective. The approach is illustrated in Fig. 19. Let us consider that, at a given time $t_0$, one of the INCUS spacecraft is observing a specific point $O^T$ on the reference ground path and imprinting a footprint at $O^F$. Since $O^T$ lies on the ground track of the virtual spacecraft, let us assume that the virtual spacecraft is positioned at the Zenith of $O^T$ at time $t_0$ (to simplify the description, we also assume a spherical Earth such that the geocentric and geodetic Zenith coincide). Starting from time $t_0$, the virtual spacecraft will move along its orbit, while the imprinted

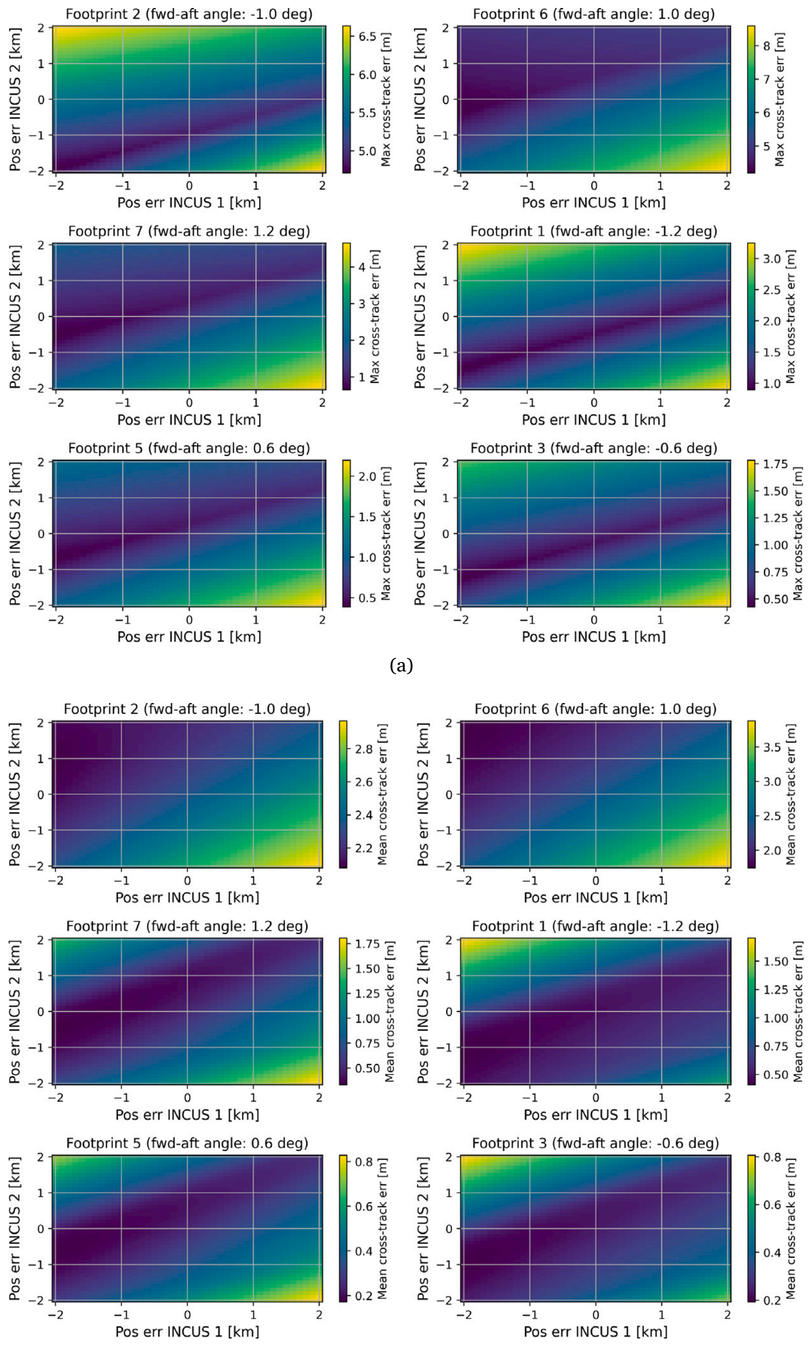

(a)

(b)

**Fig. 16.** Maximum and mean absolute cross-track multi-satellite observation error for different combinations of knowledge position errors.

footprint will move due to Earth's rotation. From this standpoint, the motion of the virtual spacecraft and the footprint can be treated separately. During this motion, it is of interest to find the time $t_1$ at which the geocentric position of the footprint is perpendicular to the earth-fixed velocity (i.e., $\mathbf{v}^e_{IT}$) direction defined at the subsatellite point of the virtual spacecraft. This approach is equivalent to find the point on the reference ground path at which the position of the footprint is perpendicular (as described in Section 4.2, but from an earth-fixed perspective). For comparison, the cross-track angle $\epsilon$ in Fig. 19 is equivalent to angle $\epsilon^{(0)}$ in Fig. 4. Notice that both represent the cross-track angle relative to the reference ground path prior to the yaw rotation.

As discussed in the following, the problem can be formalized as a system of ordinary differential equations describing the motion of the footprint relative to the inertial subsatellite trajectory of the virtual spacecraft. Both the initial and final positions of the footprint are subject to geometric constraints. At time $t_1$, the geocentric position must be perpendicular to the ground path, having the desired cross-track angle. At time $t_0$, the position must satisfy the equation of a cone, since the spacecraft can relocate the footprint only through a rotation about the yaw axis.

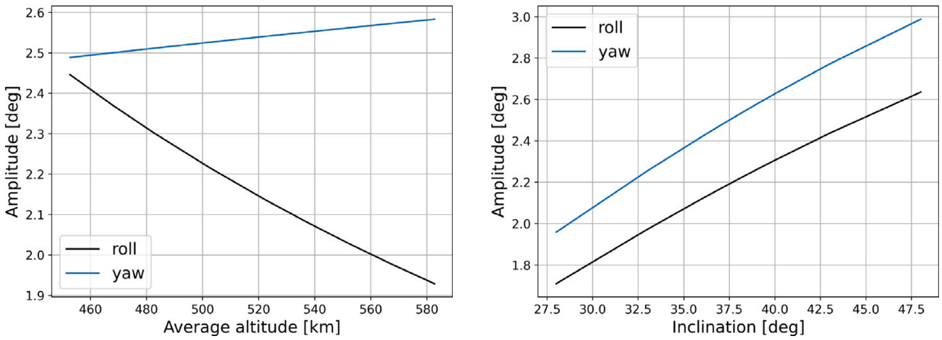

(a) (b)

**Fig. 17.** Variation in the roll and yaw amplitudes as a function of average altitude (a) and inclination (b). (For interpretation of the references to color in this figure legend, the reader is referred to the web version of this article.)

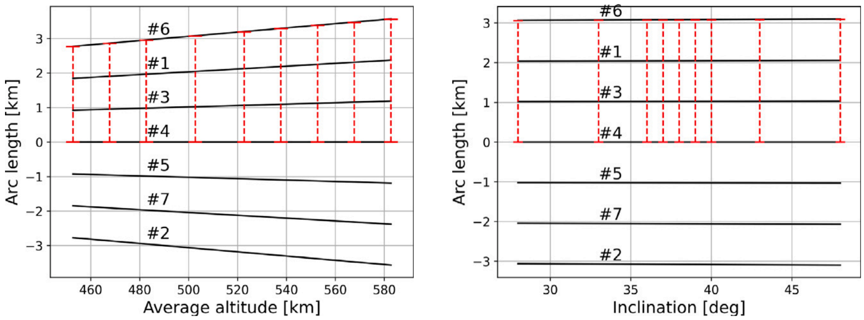

(a) (b)

**Fig. 18.** Verification of the 2/3 footprint-overlap requirement in the case of altitude (a) or inclination (b) variations. The red dashed vertical lines represent the mean footprint diameter for each considered orbit.

### *A.1. Footprint position*

Given the knowledge of the footprint's geocentric position (Section 4.1), the first step consists in locating the footprint relative to the inertial subsatellite trajectory of the virtual spacecraft (Fig. A.20). For this reason, a reference frame $F^T \triangleq \left\{O^T, \mathbf{e}^T\right\}$ is defined at each time $t_0$ as:

$$\begin{aligned} \mathbf{e}_x^T &\triangleq \mathbf{e}_y^T \times \mathbf{e}_z^T \\ \mathbf{e}_y^T &\triangleq \frac{\mathbf{e}_z^T \times \mathbf{v}_{IT}}{\left\|\mathbf{e}_z^T \times \mathbf{v}_{IT}\right\|} \\ \mathbf{e}_z^T &\triangleq \frac{\mathbf{r}_{IT}}{r_{IT}} \end{aligned} \tag{A.1}$$

where $\mathbf{v}_{IT}$ is the absolute velocity of the virtual spacecraft's subsatellite point. The inertial coordinates of $\mathbf{r}_{IT}$ and $\mathbf{v}_{IT}$ at $t_0$ can be derived as ${}^I\boldsymbol{r}_{IT,t_0} = \mathrm{T}^{IE}_{t_0}\,{}^E\boldsymbol{r}_{IT}$ and ${}^I\boldsymbol{v}_{IT,t_0} = \mathrm{T}^{IE}_{t_0}\,{}^E\boldsymbol{v}^e_{IT} + {}^I\boldsymbol{\omega}^E \times {}^I\boldsymbol{r}_{IT,t_0}$, where $\mathrm{T}^{IE}_{t_0}$ is the rotation matrix from ECEF to ECI coordinates at $t_0$, while ${}^E\boldsymbol{r}_{IT}$ and ${}^E\boldsymbol{v}^e_{IT}$ are the geocentric position and earth-fixed velocity of the subsatellite point in ECEF coordinates. As shown in Fig. A.20, the footprint's position vector $\mathbf{r}_{IF}$ can be described through a sequence of Euler angles in the along-track and cross-track directions. To this end, a second reference frame $F^{T''} \triangleq \left\{O^F, \mathbf{e}^{T''}\right\}$ is derived from $F^T$ through a Y–X sequence of rotations. Given that $\mathbf{e}_z^{T''}$ is aligned with $\mathbf{r}_{IF}$, and noting that both $\mathbf{e}_y^T$ and $\mathbf{e}_z^{T''}$ are orthogonal to $\mathbf{e}_x^{T''}$, the axes of $F^{T''}$ are defined as:

$$\begin{aligned} \mathbf{e}_x^{T''} &\triangleq \frac{\mathbf{e}_y^T \times \mathbf{e}_z^{T''}}{\left\|\mathbf{e}_y^{T''} \times \mathbf{e}_z^{T''}\right\|} \\ \mathbf{e}_y^{T''} &\triangleq \mathbf{e}_z^{T''} \times \mathbf{e}_x^{T''} \\ \mathbf{e}_z^{T''} &\triangleq \frac{\mathbf{r}_{IF}}{r_{IF}} \end{aligned} \tag{A.2}$$

By introducing the auxiliary unit vector:

$$\mathbf{e}_z^{T'} \triangleq \mathbf{e}_x^{T''} \times \mathbf{e}_y^T \tag{A.3}$$

the along-track angle relative to $F^T$ is computed as:

$$\alpha = \operatorname{atan2}\left(\mathbf{e}_z^{T'} \cdot \mathbf{e}_x^T, \mathbf{e}_z^{T'} \cdot \mathbf{e}_z^T\right) \tag{A.4}$$

while the cross-track angle relative to $F^T$ is given by:

$$\beta = \operatorname{atan2}\left(\mathbf{e}_z^{T'} \cdot \mathbf{e}_y^{T''}, \mathbf{e}_z^{T'} \cdot \mathbf{e}_z^{T''}\right) \tag{A.5}$$

### *A.2. Equations of motions*

As the footprint motion is dictated by the Earth's rotation, point $O^F$ will move, in general, in both the along-track and cross-track directions (see Fig. A.21). This motion can be described by the time derivatives of the along-track and cross-track Euler angles (namely $\alpha$ and $\beta$) defined in (A.4) and (A.5). The Euler angles rates can be related to the Earth's angular velocity $\boldsymbol{\omega}^E$ by considering a general Y–X–Z rotation sequence that superimposes frame $F^T$ onto frame $F^F$. It follows that:

$$\boldsymbol{\omega}^E = \dot{\alpha}\mathbf{e}_y^T + \dot{\beta}\mathbf{e}_x^{T''} + \dot{\eta}\mathbf{e}_z^F \tag{A.6}$$

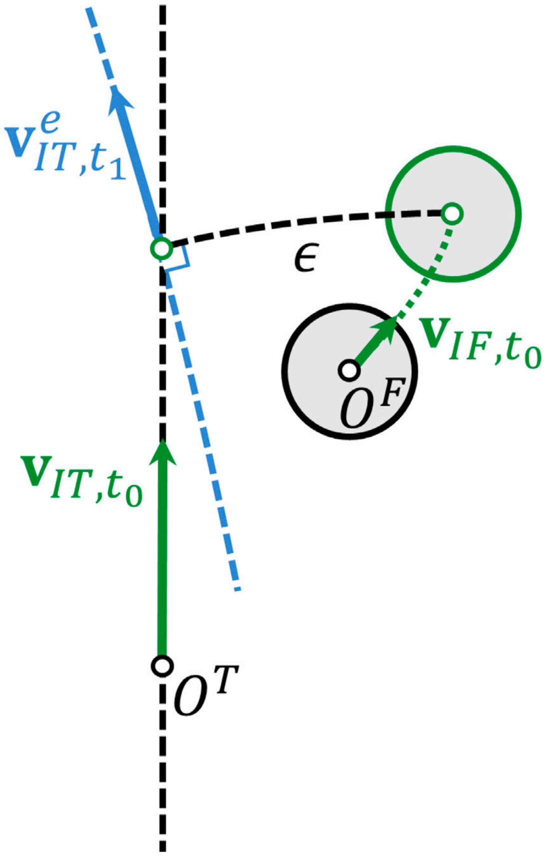

**Fig. 19.** Cross-track placement of the footprint from an inertial perspective. The black dashed line represents the inertial subsatellite trajectory of the virtual spacecraft, while the light blue dashed line indicates the virtual spacecraft's ground track at time $t_1$. The imprinted footprint at time $t_0$ is depicted as a circle with a black contour, while its position at $t_1$ is shown as a circle with a green contour. The white dots with a black contour represent the subsatellite point of the virtual spacecraft and the position of the footprint at $t_0$, respectively. The white dots with a green contour represent the same points at time $t_1$. Vectors $\mathbf{v}_{IT,t_0}$ and $\mathbf{v}_{IF,t_0}$ represent, respectively, the absolute velocity of the virtual spacecraft's subsatellite point and the footprint at time $t_0$. Vector $\mathbf{v}^{e}_{IT,t_1}$ represents the earth-fixed velocity of the virtual spacecraft's subsatellite point at time $t_1$. (For interpretation of the references to color in this figure legend, the reader is referred to the web version of this article.)

where $\dot{\alpha}$, $\dot{\beta}$ and $\dot{\eta}$ are the three unknown Euler angle rates. At the same time, the Earth's angular velocity can be expressed in the $F^F$ frame as:

$$\boldsymbol{\omega}^E = {}^F\omega^E_x \mathbf{e}^F_x + {}^F\omega^E_y \mathbf{e}^F_y + {}^F\omega^E_z \mathbf{e}^F_z \tag{A.7}$$

By performing the cross product $\boldsymbol{\omega}^E \times \mathbf{e}^F_z$ for Eqs. (A.6) and (A.7) and equating the results, we obtain:

$$\dot{\alpha} \cos\beta \mathbf{e}^{T''}_x - \dot{\beta} \mathbf{e}^{T''}_y = {}^F\omega^E_y \mathbf{e}^F_x - {}^F\omega^E_x \mathbf{e}^F_y \tag{A.8}$$

Since frame $F^F$ is obtained by rotating frame $F^{T''}$ about $\mathbf{e}^{T''}_z$ by angle $\eta$, then $\mathbf{e}^F_x = \cos\eta\, \mathbf{e}^{T''}_x + \sin\eta\, \mathbf{e}^{T''}_y$ and $\mathbf{e}^F_y = -\sin\eta\, \mathbf{e}^{T''}_x + \cos\eta\, \mathbf{e}^{T''}_y$. Substituting these equations into (A.8) results in:

$$\dot{\alpha} = \frac{1}{\cos\beta} \left( {}^F\omega^E_y \cos\eta + {}^F\omega^E_x \sin\eta \right) \tag{A.9}$$

$$\dot{\beta} = {}^F\omega^E_x \cos\eta - {}^F\omega^E_y \sin\eta \tag{A.10}$$

Similarly, the equation for $\dot{\eta}$ can be found by performing $\boldsymbol{\omega}^E \cdot \mathbf{e}^F_z$ for Eqs. (A.6) and (A.7) and equating the results:

$$-\dot{\alpha} \sin\beta + \dot{\eta} = {}^F\omega^E_z \tag{A.11}$$

The substitution of $\dot{\alpha}$ from Eq. (A.9) in the latter yields:

$$\dot{\eta} = \tan\beta \left( {}^F\omega^E_y \cos\eta + {}^F\omega^E_x \sin\eta \right) + {}^F\omega^E_z \tag{A.12}$$

Eqs. (A.9), (A.10), and (A.12) form a system of coupled ODEs that describe the time evolution of the Euler angles $\alpha$, $\beta$ and $\eta$. These equations can be written in matrix form as:

$$\begin{bmatrix} \dot{\alpha} \\ \dot{\beta} \\ \dot{\eta} \end{bmatrix} = \begin{bmatrix} \frac{\sin\eta}{\cos\beta} & \frac{\cos\eta}{\cos\beta} & 0 \\ \cos\eta & -\sin\eta & 0 \\ \tan\beta \sin\eta & \tan\beta \cos\eta & 1 \end{bmatrix} \begin{bmatrix} {}^F\omega^E_x \\ {}^F\omega^E_y \\ {}^F\omega^E_z \end{bmatrix} \tag{A.13}$$

It must be noted that $\boldsymbol{\omega}^E$ has constant components relative to $F^F$, as it defines the inertially fixed axis of rotation about which $F^F$ rotates with constant angular velocity. The integration of Eq. (A.13) yields the time evolution of the Euler angles, and thus the motion of the footprint relative to $F^T$.

The inertial subsatellite trajectory of the virtual spacecraft is approximated as a locally uniform circular motion from $t_0$ to $t_1$, dictated by the absolute velocity $\mathbf{v}_{IT,t_0}$. Assuming a spherical Earth model, the validity of this approximation depends on the orbital motion during the period $t_1 - t_0$. Although $t_1$ is not known, it can be estimated to be on the order of magnitude of $t_1 \approx \alpha_{t_0} / \omega^T$ (where $\omega^T$ is defined next). By expressing the absolute velocity of $O^T$ as $\mathbf{v}_{IT} = {}^T v_{IT,z} \mathbf{e}^T_z + \boldsymbol{\omega}^T \times \mathbf{r}_{IT}$ and cross-multiplying it by $\mathbf{r}_{IT}$, we obtain:

$$\boldsymbol{\omega}^T = \frac{\mathbf{r}_{IT} \times \mathbf{v}_{IT}}{r^2_{IT}} \tag{A.14}$$

From which it follows that the along-track motion of $O^T$ is equal to:

$$\alpha^T(t) = \omega^T (t - t_0) \tag{A.15}$$

Having described both the inertial subsatellite trajectory of the virtual spacecraft and the inertial motion of the footprint, the next step is to define the geometrical constraints at $t_0$ and $t_1$ that result in the desired cross-track placement of the footprint at $t_1$.

### A.3. Final constraint

During the inertial motion of the footprint and the virtual spacecraft, it is of interest to identify the time $t_1$ at which the geocentric position of the footprint is perpendicular to the ground track direction at $\mathbf{r}_{IT,t_1}$ (Fig. A.21). This condition is described by the following geometrical constraint:

$$\mathbf{e}^{T^*}_z(\alpha^T_{t_1}) \times \mathbf{e}^F_z(\alpha_{t_1}, \beta_{t_1}) = \sin\epsilon\, \mathbf{u}^e_{IT}(\alpha^T_{t_1}) \tag{A.16}$$

where $\mathbf{u}^e_{IT} \triangleq \mathbf{v}^e_{IT} / \|\mathbf{v}^e_{IT}\|$ describes the local ground track direction and $\epsilon$ the cross-track angle relative to it. The unit vector $\mathbf{e}^{T^*}_z$ is described by a rotation of $\mathbf{e}^T_z$ about axis $\mathbf{e}^T_y$ by an angle $\alpha^T$, thus:

$$\mathbf{e}^{T^*}_z(\alpha^T) = \sin\alpha^T \mathbf{e}^T_x + \cos\alpha^T \mathbf{e}^T_z \tag{A.17}$$

Similarly, $\mathbf{e}^F_z$ is described by a first rotation of $\mathbf{e}^T_z$ about axis $\mathbf{e}^T_y$ by an angle $\alpha$, followed by a second rotation about $\mathbf{e}^{T'}_x$ by an angle $\beta$, thus:

$$\mathbf{e}^F_z(\alpha, \beta) = \sin\alpha \cos\beta \mathbf{e}^T_x - \sin\beta \mathbf{e}^T_y + \cos\alpha \cos\beta \mathbf{e}^T_z \tag{A.18}$$

The cross-product between (A.17) and (A.18) yields:

$$\mathbf{e}^{T^*}_z(\alpha^T) \times \mathbf{e}^F_z(\alpha, \beta) = \left[\mathbf{e}^T\right] \begin{bmatrix} \cos\alpha^T \sin\beta \\ \sin\left(\alpha - \alpha^T\right) \cos\beta \\ -\sin\alpha^T \sin\beta \end{bmatrix} \tag{A.19}$$

where $\left[\mathbf{e}^T\right] \triangleq \left[\mathbf{e}^T_x \quad \mathbf{e}^T_y \quad \mathbf{e}^T_z\right]^{\top}$.

The velocity vector $\mathbf{v}^e_{IT}$, which describes the local direction of the ground track, can be expressed as a function of $\alpha^T$ by using the following relation:

$$\mathbf{v}^e_{IT}\left(\alpha^T\right) = \left(\boldsymbol{\omega}^T - \boldsymbol{\omega}^E\right) \times \mathbf{r}_{IT}\left(\alpha^T\right) \tag{A.20}$$

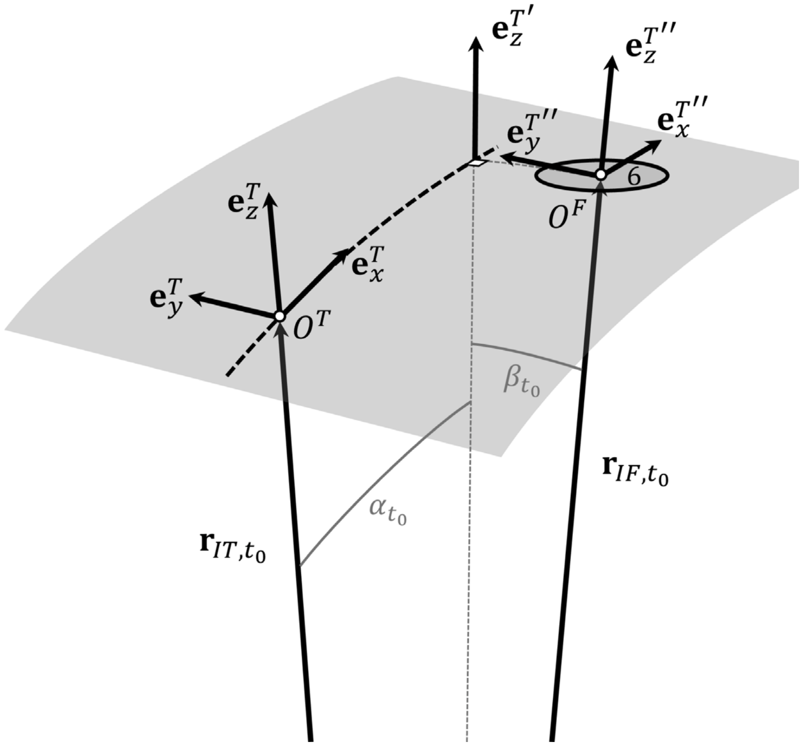

**Fig. A.20.** Footprint angular position relative to the inertial subsatellite trajectory of the virtual spacecraft (black dashed line) at time $t_0$. Footprint 6 is taken as an example of the imprinted footprint at time $t_0$. Angles $\alpha_{t_0}$ and $\beta_{t_0}$ define the angular position of the footprint relative to frame $F^T$ at the time of observation $t_0$.

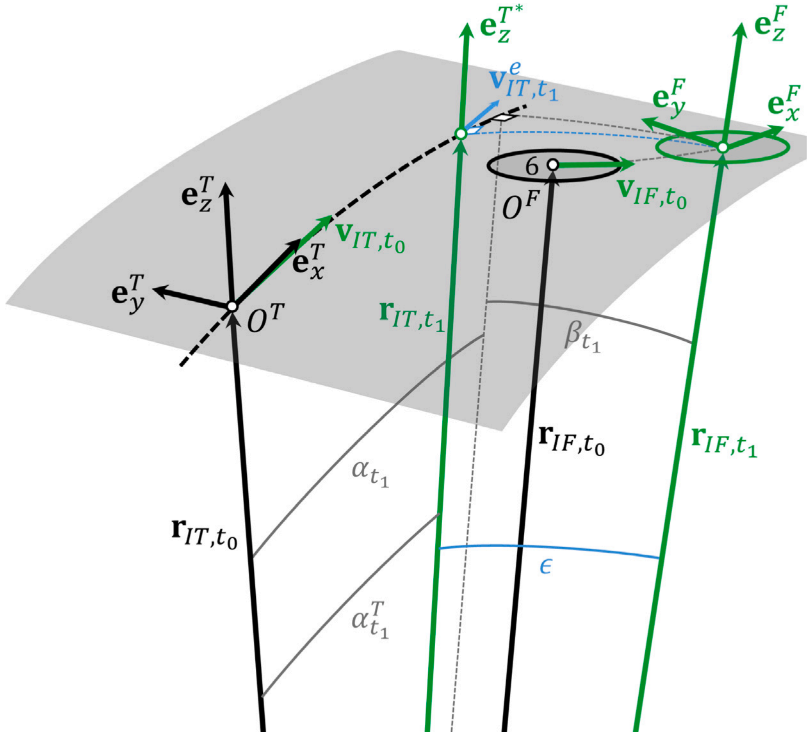

**Fig. A.21.** Inertial subsatellite trajectory of the virtual spacecraft and inertial motion of footprint 6 from time $t_0$ to $t_1$.

which relates the earth-fixed velocity of point $O^T$ to its absolute velocity. By expressing $\boldsymbol{\omega}^T$ and $\boldsymbol{\omega}^E$ in $F^T$ coordinates and substituting (A.17) into $\mathbf{r}_{IT}(\alpha^T) = r_{IT}\mathbf{e}_z^{T*}(\alpha^T)$, Eq. (A.20) rewrites as:

$$\mathbf{v}^e_{IT}\left(\alpha^T\right) = \left(\omega^T \mathbf{e}^T_y - {}^T\omega^E_x \mathbf{e}^T_x - {}^T\omega^E_y \mathbf{e}^T_y - {}^T\omega^E_z \mathbf{e}^T_z\right) \times r_{IT}\left(\sin\alpha^T \mathbf{e}^T_x + \cos\alpha^T \mathbf{e}^T_z\right) \tag{A.21}$$

Performing the cross products in (A.21) yields:

$$\mathbf{v}^e_{IT}\left(\alpha^T\right) = r_{IT}\left[\mathbf{e}^T\right]\begin{bmatrix} \cos\alpha^T\left(\omega^T - {}^T\omega^E_y\right) \\ {}^T\omega^E_x \cos\alpha^T - {}^T\omega^E_z \sin\alpha^T \\ -\sin\alpha^T\left(\omega^T - {}^T\omega^E_y\right) \end{bmatrix} \tag{A.22}$$

The substitution of (A.19) and (A.22) into (A.16) yields:

$$\begin{bmatrix} \cos\alpha^T_{t_1}\sin\beta_{t_1} \\ \sin\left(\alpha_{t_1} - \alpha^T_{t_1}\right)\cos\beta_{t_1} \\ -\sin\alpha^T_{t_1}\sin\beta_{t_1} \end{bmatrix} = \sin\epsilon \frac{r_{IT}}{\left\|\mathbf{v}^e_{IT}\left(\alpha^T_{t_1}\right)\right\|}\begin{bmatrix} \cos\alpha^T_{t_1}\left(\omega^T - {}^T\omega^E_y\right) \\ {}^T\omega^E_x \cos\alpha^T_{t_1} - {}^T\omega^E_z \sin\alpha^T_{t_1} \\ -\sin\alpha^T_{t_1}\left(\omega^T - {}^T\omega^E_y\right) \end{bmatrix} \tag{A.23}$$

The final constraint is now expressed as a function of $\alpha^T_{t_1}$, $\alpha_{t_1}$ and $\beta_{t_1}$, which are the angles at time $t_1$ resulting from the integration of (A.13) and (A.15). Note that the problem can be interpreted in two ways, depending on whether $\epsilon$ is treated as an unknown or as a given parameter. For instance, if the objective were to determine the value of $\epsilon$ at a given time $t_1$, then (A.13) and (A.15) can be used, given the initial position of the footprint $\alpha_{t_0}$ and $\beta_{t_0}$, to compute the angles $\alpha^T_{t_1}$, $\alpha_{t_1}$ and $\beta_{t_1}$, which can be then substituted into (A.23) to determine the value of $\epsilon$. However, the objective of the present analysis is more complex, as we aim for the footprint's geocentric position at $t_1$ to be both perpendicular and to form a specific angle $\epsilon$ relative to the reference ground track. This condition may be satisfied at an unknown time $t_1$ and for an unknown starting position of the footprint at $t_0$.

### *A.4. Initial constraint*

The geocentric position of the footprint at time $t_0$ can be modified to achieve the desired cross-track placement at $t_1$. However, this relocation can occur only through a yaw rotation about axis $\mathbf{e}''_z$ (see Fig. 5) due to attitude constraints. Therefore, the footprint position must satisfy the following cone equation:

$$\mathbf{u}_{BT} \cdot \left[\mathbf{r}_{IF}\left(\alpha^c_{t_0}, \beta^c_{t_0}\right) - \mathbf{r}_{IB}\right] = \left\|\mathbf{r}_{IF}\left(\alpha^c_{t_0}, \beta^c_{t_0}\right) - \mathbf{r}_{IB}\right\|\cos\gamma \tag{A.24}$$

where $\gamma$ is the fixed angle between the unit ground track pointing vector $\mathbf{u}_{BT}$ and the footprint's boresight, $\mathbf{r}_{IB}$ is the spacecraft's position at $t_0$ and $\mathbf{r}_{IF}$ is the geocentric position of the footprint. Vector $\mathbf{r}_{IF}$ can be expressed, by means of (A.18), as $\mathbf{r}_{IF} = r_{IF}\mathbf{e}^F_z\left(\alpha^c_{t_0}, \beta^c_{t_0}\right)$, where $\alpha^c_{t_0}$ and $\beta^c_{t_0}$ represent the new angular position of the footprint at $t_0$.

The solution to this problem can be summarized as determining the angles $\alpha^c_{t_0}$ and $\beta^c_{t_0}$ that satisfy the constraint Eq. (A.24), and for which angles $\alpha^T_{t_1}$, $\alpha_{t_1}$, and $\beta_{t_1}$—obtained from the integration of Eq. (A.13) and from Eq. (A.15) for a certain final time $t_1$—fulfill the cross-track placement constraint given by (A.23) with the desired angle $\epsilon_d$. The primary obstacle in obtaining a closed-form solution is that the system of ODEs (A.13) is nonlinear and involves three coupled variables ($\alpha$, $\beta$, $\gamma$), making it inherently difficult to solve analytically. Even if an analytical solution were available, it would need to be substituted into the nonlinear system of Eqs. (A.23), which must then be solved for $\alpha^c_{t_0}$ and $\beta^c_{t_0}$. At the same time, $\alpha^c_{t_0}$ and $\beta^c_{t_0}$ must satisfy the initial constraint given by (A.24). The combined nonlinearity in both the ODE system and the constraints makes it highly complex to derive a closed-form solution. Although a closed-form solution is not readily attainable — thereby motivating the use of the search strategy described in Section 4 — the presented formulation can be further investigated in future work to obtain an analytical solution.

## Appendix B

This section provides the equations needed to define the osculating sphere that best approximates the WGS84 Earth surface at any given point. First, the surface of the WGS84-ellipsoid can be defined by the following implicit function:

$$F\left({}^Ex, {}^Ey, {}^Ez\right) = \frac{{}^Ex^2 + {}^Ey^2}{a^2} + \frac{{}^Ez^2}{b^2} - 1 \tag{B.1}$$

where ${}^E\boldsymbol{r} = \left[{}^Ex, {}^Ey, {}^Ez\right]^\top$ are the ECEF coordinates of a point on the ellipsoid, while $a = 6378.137$ km is the semi-major axis and $b = a(1-f)$ is the semi-minor axis. The reciprocal flattening for the WGS84-ellipsoid is defined as $1/f = 298.257223563$ [16][Section 5.2.6]. The normal ${}^E\boldsymbol{n}$ to the WGS84-ellipsoid in ECEF coordinates is computed by taking the gradient of $F$:

$${}^E\boldsymbol{n} \equiv \nabla F\left({}^Ex, {}^Ey, {}^Ez\right) = 2\begin{bmatrix} \frac{{}^Ex}{a^2} & \frac{{}^Ey}{a^2} & \frac{{}^Ez}{b^2} \end{bmatrix}^\top \tag{B.2}$$

from which the unit normal vector is defined as ${}^E\boldsymbol{u}_{\boldsymbol{n}} = {}^E\boldsymbol{n}/\|{}^E\boldsymbol{n}\|$. The geodetic latitude follows directly from (B.2) and is computed as the arcsine of the scalar product between the unit normal and the axis aligned with the ellipsoid's semi-minor axis, that is $\varphi = \arcsin\left(2\,{}^Ez/b^2\right)$.

The local osculating sphere at a given point on the ellipsoid is defined by introducing the meridian radius of curvature, $R_M$, and the radius of curvature in the prime vertical, $R_N$ [16][Section 4.1.2]:

$$R_M(\varphi) = \frac{a(1-e^2)}{(1-e^2\sin^2\varphi)^{3/2}} \tag{B.3}$$

$$R_N(\varphi) = \frac{a}{(1-e^2\sin^2\varphi)^{1/2}} \tag{B.4}$$

where $e = \sqrt{2f - f^2}$ is the eccentricity. The mean radius of curvature of the osculating sphere can be computed as the geometric mean [16][Section 4.1.2]:

$$R_C(\varphi) = \sqrt{R_M(\varphi)R_N(\varphi)} \tag{B.5}$$

Lastly, knowing the ECEF position of a point, ${}^E\boldsymbol{r}$, the unit normal at that point, ${}^E\boldsymbol{u}_{\boldsymbol{n}}$, and the mean radius of curvature, $R_C$, the position of the center of curvature $O^C$ relative to the Earth's center $O^I$ can be determined as:

$${}^E\boldsymbol{r}_{CI} = R_C\,{}^E\boldsymbol{u}_{\boldsymbol{n}} - {}^E\boldsymbol{r} \tag{B.6}$$

## References

[1] X. Chen, W. Steyn, Y. Hashida, Ground-target tracking control of Earth-pointing satellites, in: AIAA Guidance, Navigation, and Control Conference and Exhibit, 2000, http://dx.doi.org/10.2514/6.2000-4547.

[2] Y. Lian, Y. Gao, G. Zeng, Staring imaging attitude control of small satellites, J. Guid. Control Dyn. 40 (5) (2017) 1278–1285, http://dx.doi.org/10.2514/1.G002197.

[3] F. Zhang, L. Jin, G.A. Rodrigo, An innovative satellite sunlight-reflection staring attitude control with angular velocity constraint, Aerosp. Sci. Technol. 103 (2020) 105905, http://dx.doi.org/10.1016/j.ast.2020.105905.

[4] S. Han, J. Ahn, M.-J. Tahk, Analytical staring attitude control command generation method for earth observation satellites, J. Guid. Control Dyn. 45 (7) (2022) 1347–1356, http://dx.doi.org/10.2514/1.G006041.

[5] F. Feng, R. He, W. Xu, A. Lv, Study on precise satellite attitude maneuvering strategy for ultrahigh resolution spaceborne SAR imaging, IEEE Access 9 (2021) 127226–127239, http://dx.doi.org/10.1109/ACCESS.2021.3111193.

[6] H. Kim, J. Park, Y.-K. Chang, S.-H. Lee, Optimal attitude maneuvering analyses for imaging at squint staring and sliding spotlight modes of SAR satellite, Aerosp. 8 (10) (2021) http://dx.doi.org/10.3390/aerospace8100277.

[7] A. Carbone, D. Spiller, F. Curti, Analytical attitude guidance planner for multiple ground targets acquisitions, Symmetry 14 (11) (2022) http://dx.doi.org/10.3390/sym14112341.

[8] S. Tanelli, Z.S. Haddad, S. van den Heever, Investigation of convective updrafts (INCUS): status after phase A, in: S.R. Babu, T.S. Pagano, J.J. Puschell (Eds.), CubeSats, SmallSats, and Hosted Payloads for Remote Sensing VII, Vol. 12689, SPIE, International Society for Optics and Photonics, 2023, 1268904, http://dx.doi.org/10.1117/12.2677734.

[9] S. Prasanth, Z.S. Haddad, R.C. Sawaya, O.O. Sy, M. van den Heever, T. Narayana Rao, S. Hristova-Veleva, Quantifying the vertical transport in convective storms using time sequences of radar reflectivity observations, J. Geophys. Res.: Atmospheres 128 (10) (2023) e2022JD037701, http://dx.doi.org/10.1029/2022JD037701, e2022JD037701 2022JD037701.

[10] G. Gupta, A. Mancini, P. Focardi, Preliminary feed assembly design for INCUS, in: 2023 IEEE Wireless Antenna and Microwave Symposium, WAMS, 2023, pp. 1–5, http://dx.doi.org/10.1109/WAMS57261.2023.10242936.

[11] Z.S. Haddad, R.C. Sawaya, S. Prasanth, M. van den Heever, O.O. Sy, C. van den Heever, L.D. Grant, T.N. Rao, G.L. Stephens, S. Hristova-Veleva, D.J. Posselt, R.L. Storer, Observation strategy of the incus mission: Retrieving vertical mass flux in convective updrafts from low-earth-orbit convoys of miniaturized microwave instruments, in: IGARSS 2022 - 2022 IEEE International Geoscience and Remote Sensing Symposium, 2022, pp. 6448–6451, http://dx.doi.org/10.1109/IGARSS46834.2022.9884264.

[12] K. Boudad, Q. Kostelecky, Relative phasing and observations overlap: Low-thrust trajectory design options for the incus mission, in: 33rd AAS/AIAA Space Flight Mechanics Meeting, 2023.

[13] B. Donitz, A. Austin, L. Yam, V. Torossian, S. Durden, J. Beatty, J. Siles, D. Penrod, Q. Kostelecky, S. Tanelli, Y. Kim, Baseline design of the investigation of convective updrafts (INCUS) mission, in: 2024 IEEE Aerospace Conference, 2024, pp. 1–9, http://dx.doi.org/10.1109/AERO58975.2024.10521166.

[14] A.A. Shabana, Dynamics of Multibody Systems, Cambridge University Press, 2020.

[15] B. Rhodes, Skyfield: High Precision Research-Grade Positions for Planets and Earth Satellites Generator, Astrophysics Source Code Library, 2019, record ascl:1907.024.

[16] W. Torge, J. Müller, R. Pail, Geodesy, De Gruyter Oldenbourg, Berlin, Boston, 2023, http://dx.doi.org/10.1515/9783110723304, [cited 2025-11-20].